Experimental study and analysis of a novel layered packed-bed for thermal energy storage applications: A proof of concept

Muhammad Tahir Ameen [a,b], Zhiwei Ma [c,*], Andrew Smallbone [c], Rosemary Norman [a], Anthony Paul Roskilly [c]

[a] *School of Engineering, Newcastle University, Newcastle upon Tyne NE1 7RU, United Kingdom*
[b] *Department of Mechanical Engineering, University of Engineering and Technology, Lahore 54890, Pakistan*
[c] *Department of Engineering, Durham University, Durham DH1 3LE, United Kingdom*

ABSTRACT

This paper presents a study carried out as part of commissioning and testing of world's first grid-scale 150 kW$_e$ Pumped Heat Energy Storage (PHES) demonstration system. The system employs two novel layered packed-bed thermal stores. The present study experimentally investigates one of the stores designated as "hot thermal store", which has an energy storage density of 1072 MJ/m^3 and stores heat at 500 °C and 12 bar. The layered store is an enhancement of a normal packed-bed store and offers a higher degree of thermal stratification. Experiments show that layering results in about 64 % reduction in pressure loss along with yielding considerably narrower thermocline. Round-trip efficiency, storage capacity and utilisation were calculated based on 1st Law analysis considering both simple and layered mode operation at nominal design conditions. Two cycle control scenarios were considered: time-based and temperature-based. In the time-based scenario, the store shows nearly similar performance in both modes. However, in temperature-based scenario, layered mode outperforms. During cyclic operation, layered mode outperforms as it reaches steady-state in merely 3rd cycle, without any loss in efficiency, capacity and utilisation; simple mode yields competitive efficiency but capacity and utilisation deteriorate after each successive cycle and steady-state is achieved in 20th cycle. 2nd Law analysis was additionally performed to gain insight into various losses and their impact on the performance.

1. Introduction

1.1. Energy storage needs

The capacity of renewable energy (RE) around the world has doubled over the last 10 years due to cost reductions and supportive policies [1]. Technology advances and prompted market competition are likely to motivate further deployment of renewable installations across the globe. It is predicted that the share of RE in the worldwide total primary energy supply would increase from 14 % in 2015 to 63 % in 2050, whilst the share solely in the power sector over the same period would increase from 25 % to 85 % [2]. Therefore, renewable generators, such as onshore and offshore wind farms, concentrated solar power (CSP) and photovoltaic (PV) arrays, are seen as the future of next-generation electrical power systems.

RE offers variable and fluctuating power [3,4]. This pivotal drawback calls for a more flexible, dynamic power system enabled via pairing of an energy storage (ES) facility with clean, renewable generation [5,6]. As such, an ES system is essential to act as a 'buffer' between the RE supply and the demand, allowing greater grid stability by adjusting the load and power quality [7,8]. Much like the trends of RE, ES installations are increasing exponentially [9]. As of mid-2017, worldwide installed ES capacity stood at nearly 176 GW [10] and the annual battery storage deployment increased from 3.3 GW in 2019 to 5.0 GW in 2020 [11]. Geographically constrained pumped hydropower storage (PHS), currently dominating with 96 % share of the total capacity of ES, will be superseded by newer ES systems to develop a more decentralised power system. Even though battery storage, behind-the-meter in particular, is being promoted, it is still an expensive option due to high upfront costs, and faces recycling challenges. Therefore, to fulfil the ramped-up ES demand, other means than the 'traditional and expensive' kinds will have to be explored.

Nomenclature

A	store cross-sectional area, m^2
B	exergy, J
Bi	Biot number, –
C_d	discharge coefficient, –
c_p	gas isobaric specific heat capacity, J.kg^{-1}.K^{-1}
c_s	solid specific heat capacity, J.kg^{-1}.K^{-1}
d	diameter, m
D	store diameter, m
d_p	particle diameter, m
f	friction factor, –
G	mass flux, kg.s^{-1}.m^{-2}
h	convective heat transfer coefficient, W.m^{-2}.K^{-1}
k_g	gas thermal conductivity, W.m^{-1}.K^{-1}
l	length scale, m
L	store length, m
$\dot{m}_g$	gas mass flow rate, kg.s^{-1}
m_s	solid mass, kg, ton
Nu	Nusselt number, –
p	gas pressure, Pa, bar
Pr	Prandtl number, –
Q	rate of heat transfer, W
R	gas constant, J.kg^{-1}.K^{-1}
Re	Reynolds number, –
RTE	round-trip efficiency, %
S	rate of entropy generation, J.K^{-1}.s^{-1}
SC	storage capacity, kW.h
S_v	particle surface area-to-volume ratio, m^{-1}
T	temperature, °C, K
t	time, s, hr
t_N	nominal charge time, hr
U	gas flow velocity, m.s^{-1}; store utilisation, %
U_o	open-tube gas flow velocity, m.s^{-1}
V	store volume, m^3

z	store axial distance, m

Greek letters

β	ratio of diameters, –
ε	store void fraction, –
ζ	exergetic loss coefficient, %
η	dimensionless time variable
μ_g	gas dynamic viscosity, Pa.s
ξ	dimensionless length variable
ρ	density, kg.m^{-3}
ρ_{ES}	energy storage density, J.m^{-3}
τ	time scale, s

Subscripts

c, d	charge, discharge
g, s	gas, solid
p, m	pressure; particle, modified
t	thermodynamic, thermal
x	exit
$1, 2$	upstream and downstream conditions; 1st Law and 2nd Law

Abbreviations

CAES	compressed air energy storage
CSP	concentrated solar power
ES	energy storage
HP	heat pump
HTF	heat transfer fluid
LAES	liquid air energy storage
LCS	layer control system
MCS	main control system
PCM	phase-change material
PHES	pumped heat energy storage
PHS	pumped hydropower storage
PV	photovoltaic
SAH	solar air heater
RE	renewable energy
TES	thermal energy storage

1.2. Packed-bed storage and recent advances

Among the wide array of ES systems, thermal energy storage (TES) is an attractive option as it can meet both heating and cooling demands along with providing electrical energy if coupled with power generation system. It works by storing energy by changing the temperature of a suitable storage, or heat transfer substance (*e.g.,* rock, metal, salt, oil, water or phase-change material (PCM) *etc.*). There is a massive potential for TES as many dormant concepts of the past, such as pumped heat energy storage (PHES), have started to receive attention now due to technically advanced methods with reduced levelized costs [12]. TES can be categorised in three normal modes: sensible, latent and thermochemical [13–15]. A combination of sensible and latent heat storage can also be used [16]. TES with a packed-bed is an easy solution as it can adapt to each of these modes.

Solid packed-bed TES using a sensible heat method is widely used especially for high temperature heat storage. Basically, a packed-bed store is an insulated container filled with spherically or randomly shaped solid particles. Heat is stored when a high temperature heat transfer fluid (HTF) is passed through the voids of the packing, transferring its thermal energy to the solid. Conversely, the stored heat is retrieved by passing a low temperature HTF in the opposite direction. Downward flow of HTF during charge and upward during discharge usually results in better performance [17]. An important feature of the packed-bed store is the formation of a temperature gradient zone, known as 'thermocline' [18], and hence it is often called a thermocline store.

Common to many industries, packed-bed storage has established

itself as a low-cost, safe, structurally simple yet thermodynamically reliable technology [19–21]. That is why special interest is shown in studying its different configurations largely based on the state of the storage medium, mechanism of storage process and level of storage. The majority of scientific publications on packed-bed stores deal with cases where they are either integrated into CSP [22–24], solar air heater (SAH) [25–27], adiabatic compressed air energy storage (CAES) [28–30], PHES [31–33], liquid air energy storage (LAES) [34] or domestic heat pump (HP) [35] systems, thus demonstrating their wide-range capabilities. Fig. 1 illustrates packed-bed TES in several applications.

The research domain on packed-bed storage is vast, covering analytical, experimental, parametric and optimisation studies. Most studies involve performance evaluations by observing variation in a) physical design parameters: such as aspect ratio, void fraction, type, size and shape of filler materials and insulation thickness [21,27,36,37], b) HTF type and flow rate [18,38–41], c) axis of flow (*i.e.,* axial or radial) [42], or d) charge temperature [17,43]. All these affect the storage thermal response greatly. The storage performance or efficiency is mainly governed by the thermocline behaviour, which is arguably the most studied aspect as it affects exergetic efficiency: narrow thermocline results in better efficiency [44]. In spite of significant efforts to achieve an optimal behaviour, two key issues still remain a substantial challenge for the research community: a) maintaining a thin 'thermocline' and b) reducing 'pressure drop'.

A survey of literature reveals that, to date, most studies on packed-bed storage have been undertaken within the scope of 'solar' energy,
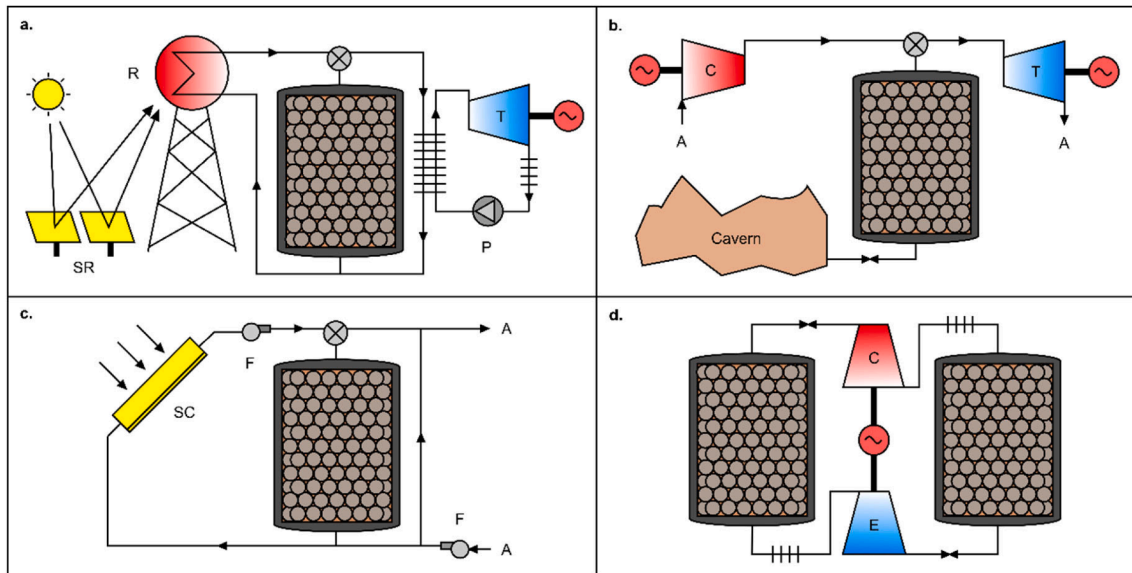
Fig. 1. Various implementations of packed-bed TES. **a.** CSP, **b.** adiabatic CAES, **c.** SAH, and **d.** PHES. Key: A – Air, C – Compressor, E – Expander, F – Fan, P – Pump, R – Receiver, SC – Solar Collector, SR – Solar Reflector, T – Turbine.

also evident from previous review studies [27,45]. In CSP applications, packed-beds are regarded as a promising alternative to the expensive two-tank molten-salt technology. In addition, they benefit from having twice the energy density, with most having about 180–250 MJ/m^3 when there is a temperature difference of 100 °C [45]. Notwithstanding, packed-bed storage has also been investigated for implementation in a variety of other power-to-heat or power-to-power applications. Many studies have focused on the selection of appropriate storage material for sensible packed-bed TES. For instance, Al-Azawii, *et al.* [46] experimentally compared the performance of recycled ceramic materials with that of conventional alumina materials in terms of thermal and pressure drop losses. The results revealed that alumina has superior thermal performance than ceramic materials, however, exergy losses due to pressure drop are higher for alumina comparatively. Kocak, *et al.* [47] tested demolition waste-based storage materials in a laboratory-scale packed-bed TES system for industrial solar applications below 200 °C. A smooth stratification behaviour of the store was observed with energy efficiency reaching as high as 67 % at a charging temperature of 150 °C. When compared with Therminol 66 synthetic oil as storage medium, demolition waste resulted in 45 % higher amount of energy stored and 60 % cost reduction. Lai, *et al.* [48] considered sintered ore particles to study the effect of several parameters on the thermal stratification performance of the packed-bed storage using air as HTF. The study concluded that small particle sinter bed yields superior thermal stratification and under steady-state cyclic operation the cycle efficiency can reach up to 66.78 %.

Various designs and combinations have been suggested in the literature in an attempt to improve storage performance. In contrast to commonplace cylindrical shapes, a truncated conical design was studied in an air-rock based pilot-scale demonstrator [49], as a means to minimise thermo-mechanical stresses. However, an optimisation study [37] revealed that a design with negative cone angle, as opposed to the positive angle in the above study, has higher exergy efficiency. Nevertheless, due to increased benefits, Singh, *et al.* [50] considered the shape with a positive cone angle and numerically investigated transient performance of a large-scale storage unit. Knobloch, *et al.* [51] presented a study on the construction and testing of a high-temperature (675 °C), 1 MWh$_t$ rock bed storage pilot plant using air as HTF. The noteworthy design feature was the packed-bed storage being partially underground with a vertical air flow configuration. By increasing the air flow rate during discharging, an improved round-trip efficiency (RTE) of 80.7 %

was achieved. Furthermore, McTigue, *et al.* [42] discussed thermodynamics of a radial-flow design for packed-beds in comparison with typical axial-flow designs mentioned above, and inferred that radial-flow design achieves lower pressure losses but results in higher capital costs due to added volume required for bypass flows. Such radial-flow design has been introduced and tested recently in the form of a laboratory-scale prototype [52]. The packed-bed had an energy capacity of 49.7 kWh$_t$ and was able to operate between 25 °C and 700 °C using dry air. The system resulted in reduced pressure losses (<1 mbar) and about 1.11 % dwell period thermal losses with an overall thermal efficiency of 71.8 %. Even so with these designs, maintaining invariable discharge temperature, which is another performance requirement, still remained as a question. Rodrigues, *et al.* [53] addressed this particular problem and emphasized only on the discharge cycle effectiveness of an air-rock packed-bed system subjected to variation in mass flow rate and storage material characteristics. Their results showed that increasing the mass flow rate and porosity improves thermal stratification and discharge cycle efficiency compared with the charge cycle. In a multi-criteria optimisation study, Roux, *et al.* [54] investigated an air-ceramic packed-bed with respect to exergy efficiency and environmental impact using life cycle assessment parameters. The results showed that exergy efficiency optimisation requires a tapered shape packed-bed whereas life cycle assessment optimisation will require a square shaped packed-bed. The study finally proposed an optimal design capable of achieving 97 % exergy efficiency. Wang, *et al.* [55] considered an array of multiple hot and cold packed-bed TES units for use in a large-scale (80 MWh) PHES system with the aim to decrease power variation during discharging. The devised arrangement, in the form of multiple TES units connected in series, resulted in a RTE of about 65 % with delivery power variation of 43.1 % which was further brought down to 13.2 % using a temperature complementation operation mode. Sensible packed-bed stores can also be implemented in PHES systems using direct and indirect approach, as in [56], where it was indicated that indirect use of packed-beds *i.e.,* through heat exchangers, the PHES system becomes advantageous in terms of reduced installation cost (by 40 %) which is realised with a minor RTE penalty (<5%). Using sensible packed-bed TES systems, Zhang, *et al.* [57] performed parametric optimization and thermo-economic analysis of Joule-Brayton cycle-based PHES system. The study showed that for a 60 MWh system, a RTE of 70.97 % can be achieved. It was noted that with an increase in charging/ discharging durations, the economic performance of the system

improves, and the aspect ratio (length-to-diameter ratio) increases for cold store whereas it decreases for hot store after an initial increase.

As a way to mitigate the problem of discharge temperature (and thus the discharge power) gradually decreasing, different options were explored: such as cascading using different PCMs, and multi-layering using both solid material and PCM. In a follow-up study, Zanganeh, *et al.* [58] suggested such a configuration which combined sensible and latent heat storage in that a small amount of PCM was added at the top of the bed with the aim to stabilise discharge temperature. The results indicated that a PCM volume of 1.33 % of the total volume was enough to keep the discharge temperature constant, however, no improvement in overall efficiency was noticed. This arrangement was studied further by Galione, *et al.* [59] who pointed out that such a method can reduce thermocline degradation over time in a cyclic operation for CSP plants. Cheng, *et al.* [60] carried out an optimisation study on a cascaded cool TES using a variable number of PCM layers, and found that cascading reduces charge time whereas storage quality and quantity are not affected compared with single-stage (layer) storage. Liu, *et al.* [61] proposed a latent packed-bed TES system incorporating three-stage PCM and three-layered diameter capsules in an attempt to improve stratification during charging. It was reported that compared with the conventional non-cascaded packed-bed with single-layered diameter capsules, the charging efficiency of the cascaded packed-bed having three-layered diameter capsules improved significantly from 24 % to 61 %. Osterman, *et al.* [62] conducted a study on a hybrid (sensible/latent) packed-bed TES system to examine the effect of PCM fraction on discharge temperature stabilization and found that increasing the PCM fraction leads to longer stabilization periods but lower initial discharge temperatures. Xue, *et al.* [63] employed two latent heat packed-bed TES units, one hot and one cold, in a hypothetical 150 kW PHES system. According to the results of their analysis, addition of recuperation between the hot store and expander decreases input power requirement by 18.1 kW and compared with sensible heat-based storage, PCM based storage increases energy density by 65 kWh/m^3.

All in all, the focus of new research has been on improving thermocline behaviour and resulting exergy efficiency by incorporating different variations to either the existing design or the HTF flow pattern inside the packed-bed. One approach, upon which the present work is based, is splitting the sensible heat-based packed-bed into a number of designated segments along its vertical axis. In published literature, this idea seems to have been coined by Crandall, *et al.* [64] and later adopted by Howes, *et al.* [65] who shaped the concept further to serve another but similar purpose, specifically for large-scale ES systems. A comparable technique was proposed around the same time by Bindra, *et al.* [66] under the name of the 'sliding flow method' to improve exergy efficiency. The method allowed the inlet and exit air flow ports of the packed-bed to change axially to follow the thermal front in the bed. However, improvement in exergy efficiency was only numerically justified, and no supporting experimental evidence can be found in the literature. Mathur, *et al.* [67] developed a method which was comprised of multiple extraction points along the bed length so that after identifying the thermocline region, the HTF could be heated up to the desired temperature via external means and then returned back at a location ahead of the thermocline movement.

Very recently, Al-Azawii, *et al.* [39] developed another new technique. They used the same term in their work *i.e.,* layered store, however, the method was different to [64,65,68] as division of the store domain was achieved by using pipes (for HTF injection) of different lengths inserted along the axis of the bed and radially separated from each other. The exergy efficiency was shown experimentally to increase from 55.4 % to 80.3 % by using three layers. Geissbühler, *et al.* [69,70] assessed different thermocline control strategies (some of which are based on the above studies), and proposed a new way named the mixing method: the HTF is extracted simultaneously from one port located at mid-height of the store and the bottom during charge (or the top during discharge) and mixed together to achieve a certain outflow temperature.

Through numerical simulations, it was shown that storage utilisation can be increased via the mixing method but this occurs at a minor efficiency penalty. Stressing the need for optimal discharge temperature (instead of thermocline degradation), another study [71] numerically examined a previously developed extraction method [67] by using multiple equidistant extraction ports although this approach differed from the one reported earlier as instead of returning the HTF back to the storage unit, it is transferred to the power block.

1.3. Present work

The aim of the present study is to address the main challenges of inconsistent output temperature during discharging due to degradation of thermal stratification and pressure drop losses incurred in a sensible packed-bed TES system. The study relates to an innovative layered packed-bed TES system which was designed according to the scheme devised by Howes, *et al.* [65] for application in a PHES system. Using the novel concept of layering in two thermal stores, one hot and one cold, a closed Joule-Brayton cycle-based system was built to demonstrate the PHES technology. The present study is primarily based on the experimental work conducted on the hot thermal store specifically designed and fabricated for this purpose. A detailed and comprehensive optimisation study was conducted by developing a numerical packed-bed model prior to the construction of the layered store. During the initial analysis, particular focus was given to the selection of appropriate storage material and optimisation of the number of layers to be constructed for given diameter and length of the store. The study involved estimation of required level of insulation and determining the thermal front control strategy and associated layer control system needed to improve temperature stratification and make best use of the layered structure. CFD analysis was additionally conducted during the research and design phase to gain in-depth insight of the layered hot store and its components of critical nature. An experimental rig was set up around the same time during the development and commissioning phase of the 150 kW$_e$ PHES demonstrator to investigate and validate the thermodynamic performance of layered hot store which is crucial for any ES system. Over the years, only one research group [36,72,73] has studied a layered design in detail, and highlighted various aspects using a numerical approach. Although important, those analyses were only theoretical and optimisation-based, and therefore, no study has been found to have provided experimental evidence to support this new concept. Featuring such a novel design, the current study examines the store performance experimentally with particular focus on thermocline behaviour, pressure losses, store utilisation and 1st and 2nd Law storage cycle efficiencies. In compliance with the target performance indicators set at the design stage, the proposed solution results in reduced pressure drop losses, enhanced temperature stratification and stable discharge temperature for relatively longer duration. The novelty of the idea is thus validated through the experimental tests and results which will fill a major gap in the existing literature in this field of technology.

2. Methodology

This section covers the description of the layered thermal store, layer control, experimental setup and the relevant instrumentation and control systems.

2.1. Thermal store design

As stated before, after carrying out numerical optimization analysis, a bespoke thermal store was designed and experimentally investigated in the present work. The store is technically advanced and offers an economical solution as an ES device. Fig. 2 shows different drawing views of the store and highlights its crucial features. The store consists of a large, vertical carbon steel pressure vessel (design code: PD5500:2009 Cat. 2 and PED Module G). It has semi-elliptical ends and is composed of
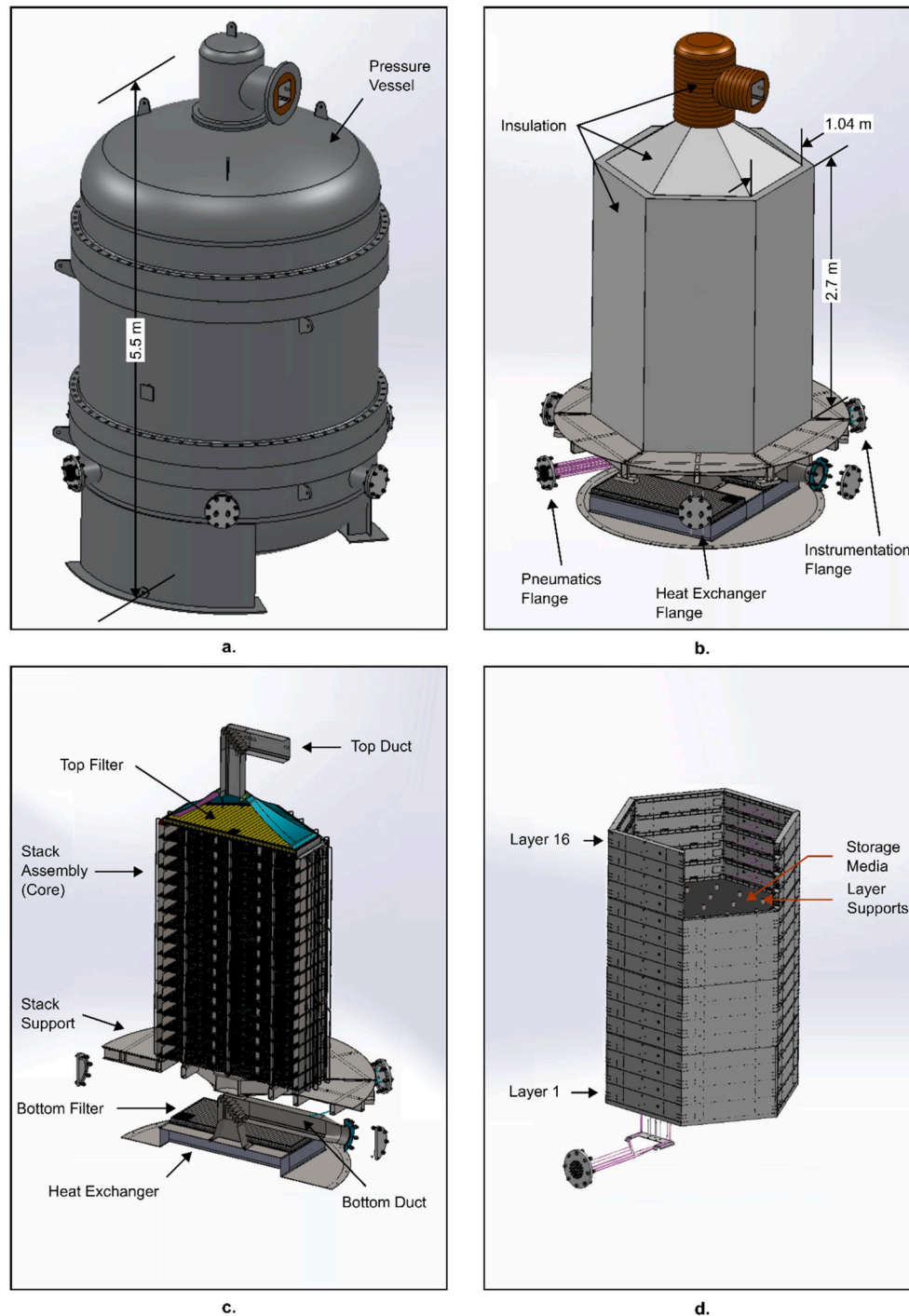
Fig. 2. 3D drawing views of the store. **a.** Complete store, **b.** Without pressure vessel, hard insulation is shown only, **c.** Section through the store with complete insulation removed, and **d.** Main core showing stack built up to layer 11.

four sections: a base with split skirt type supports, a centre section, an upper head, and a top cap attached to the upper head. These sections are connected together using bolted flanges. This vessel has a design pressure of 12.2 bar (gauge), shell internal diameter of 3 m, wall thickness of 12 mm and an overall height of 5.5 m. The internal volume of the vessel is 28.4 m^3. The vessel was hydro-tested by the supplier (Halton Fabrications ltd.).

The actual storage volume where heat is to be stored is a modular core and is present inside the vessel, separated by a layer of insulation, as shown in Fig. 2b. A fine grade of washed, dried and surface hardened magnetite (86 % Fe$_3$O$_4$ by volume containing small traces of silica) was

used as storage media. Magnetite was chosen as it is low cost, abundant and has high volumetric heat capacity [31,74,75]. The magnetite was supplied by LKAB Minerals in pebble form with an equivalent particle diameter of 2.1 mm. Atmospheric air was used as the HTF in this study. The core is a 2.7 m tall fabricated steel structure of hexagonal cross-section having a circumradius of 0.9 m. The core is divided into 16 identical, horizontal layers built successively on top of each other in the vertical direction, contained by stack panels, thus forming a stack assembly. Each layer is filled with approximately 850 kg of storage media uniformly distributed up to a depth of 111 mm. As shown in Fig. 2(c & d) (and highlighted in Fig. 7a), the construction of the layers is such that

two consecutive layers are 60 mm apart and have a free space of 36 mm for the lateral distribution of the gas over the storage media. Each layer has a 24 mm thick base which is made of an array of equilateral triangular tiles (having a side length of 300 mm) joined together. These tiles have a pattern of holes allowing the gas to pass through the base into the layer below (or above). The holes were kept much larger than the mean particle size to minimise resistance to the gas flow. A fine stainless steel 900 μm mesh, therefore, was placed above the base to prevent particles from falling through to the layer below. A number of vertical posts provide support (for the layer above) and separate the adjoining layers. By building the store in this way the weight of the upper layers is carried down through the structure by the vertical posts (under compression load only) and the base of each layer only supports the weight of the storage media in that particular layer thus reducing bending loads on the base structure. Moreover, due to the triangular geometry of the tiles, a regular hexagonal base can be developed easily which effectively fits within the cylindrical vessel thereby giving a nearly circular shaped packed-bed. Such a modular structure of the layered store, consisting of many smaller components assembled together, was used to provide mechanical stability and allow for ease of transportation and rapid construction for current and future TES systems.

The store has a number of nozzles for ancillary systems such as pressure relief, instrumentation, heat exchanger, layer control and drain systems. All connections to the store are via flanged joints. The top and bottom gas connections are made via 18″ and 8″ nozzles (ANSI 150#) respectively. Around bends, these ducts are provided with turning vanes to minimise gas flow losses. The conical section at the top of the store has flow distributors to provide even gas flow over the cross-section. The vessel is internally insulated to retain the heat within the core. The top head is the high-temperature end of the store and is insulated along with the stack walls. Two layers of 50 mm thick WDS® Ultra microporous insulation panels are attached to the top head, conical gas diffuser area and the stack walls using stainless steel straps followed by fabric sleeve fitted over the entire stack and the conical area. The surrounding region between the stack and the vessel is then loosely filled with silvapor (perlite) granules. Through simulations during design phase, it was estimated that with this insulation strategy, under a fully charged state,[1] the temperature at the pressure vessel surface is<40 °C at an ambient temperature of 20 °C. Two filter trays are fitted to the top and bottom of the store to ensure that the dust particles of the storage media do not leave the store in either direction. Both filters are made of fabricated stainless steel frames with pleated Cadisch Hollander 165/800 20 μm filtration papers. In addition, a heat exchanger is placed within the store near the bottom head to bring the exit gas temperature down to ambient during charge if required. It must be noted that this heat exchanger system was not used in the current experimentation as the store was not connected to the demonstrator. The key system parameters most relevant for the validation of developed mathematical models using experimental results and further system simulations are summarised in Table 1.

2.2. Layer control system

The most innovative feature of the store is layering. Precise control of the thermal front through the layers is achieved by selectively opening or closing of the gas bypass choke valves. A simple illustration of this situation is shown in Fig. 3. Chock valves are positioned horizontally around the edges of the hexagonal stack at every layer, as shown in a schematic figure, Fig. 4 (and photograph in Fig. 7b). Such peripherally

---

[1] Here, the fully charged state means that the store is charged to 500 °C which is the actual design temperature for use in the PHES demonstrator. However, during the current work the store was charged to a lower temperature rendering minimal thermal losses to the surroundings which, therefore, have not been included in the numerical model for validation of results.

Table 1
Fixed design parameters of the store.

Storage media	86 % Fe$_3$O$_4$: 14 % SiO$_2$
Equivalent particle diameter, d_p [mm]	2.1
Void fraction, ε [–]	0.425
Bulk density [a,] ρ_s [kg.m^{-3}]	4800
Bulk specific heat capacity, c_s [J.kg^{-1}.K^{-1}]	See *Sec.* 3.4
Total mass, m_s [ton]	13.6
Thermal store	
Diameter [b,] D [m]	1.88
Length [b,] L [m]	1.776
Volume [b,] V [m^3]	4.93
Number of layers	16
Energy storage density, $\rho_{ES} = \rho_s c_s (1 - \varepsilon) \Delta T / V$ [MJ.m^{-3}]	1072

[a] Density of pure magnetite is 5150 kg/m^3. However, due to the presence of small impurity in the form of silica, bulk density has been calculated and used in the numerical analysis.
[b] These are equivalent dimensions and have been determined by considering the store to be of a perfect circular cross-section and assuming that there are no gas gaps between successive layers *i.e.*, a case of simple store.
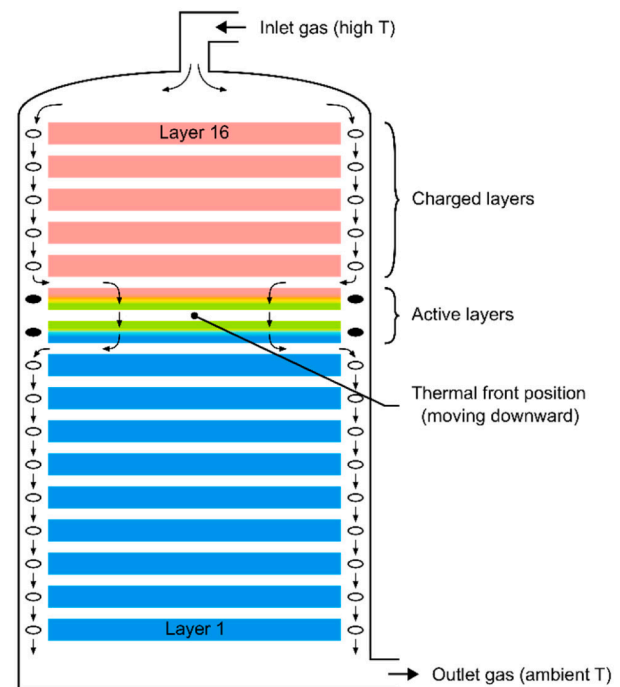
Fig. 3. Gas passage through the active layers of the layered store during charge. Thermal front is confined to only two layers, 10 and 11, where the side valves are closed (shown in black).

located valves provide a sufficiently uniform flow distribution through the active layers *i.e.,* layers where significant heat transfer is taking place. When the valves at a particular layer are open, the porosity through the storage media at that layer is reduced and the gas circumvents the layer. Conversely, when the valves at a particular layer are closed, the gas is forced to pass through the media of the layer.

Fig. 4 presents the schematic layout of the hardware of an intelligent Layer Control System (LCS) which is responsible for the thermal front control in the layered store. The LCS consists of two subsystems which are internal and external to the store. The internal subsystem comprises of choke valves and corresponding actuation mechanism whereas the external subsystem comprises of 4-port valves and their corresponding control mechanism (photographs are shown in Fig. 5(a & b)). As shown in Fig. 4, there are 6 sets of choke valves in every layer, each accommodating in one side of the hexagon. A single choke valve is made of 9 pucks, attached to a common rail, and translates over as many circular
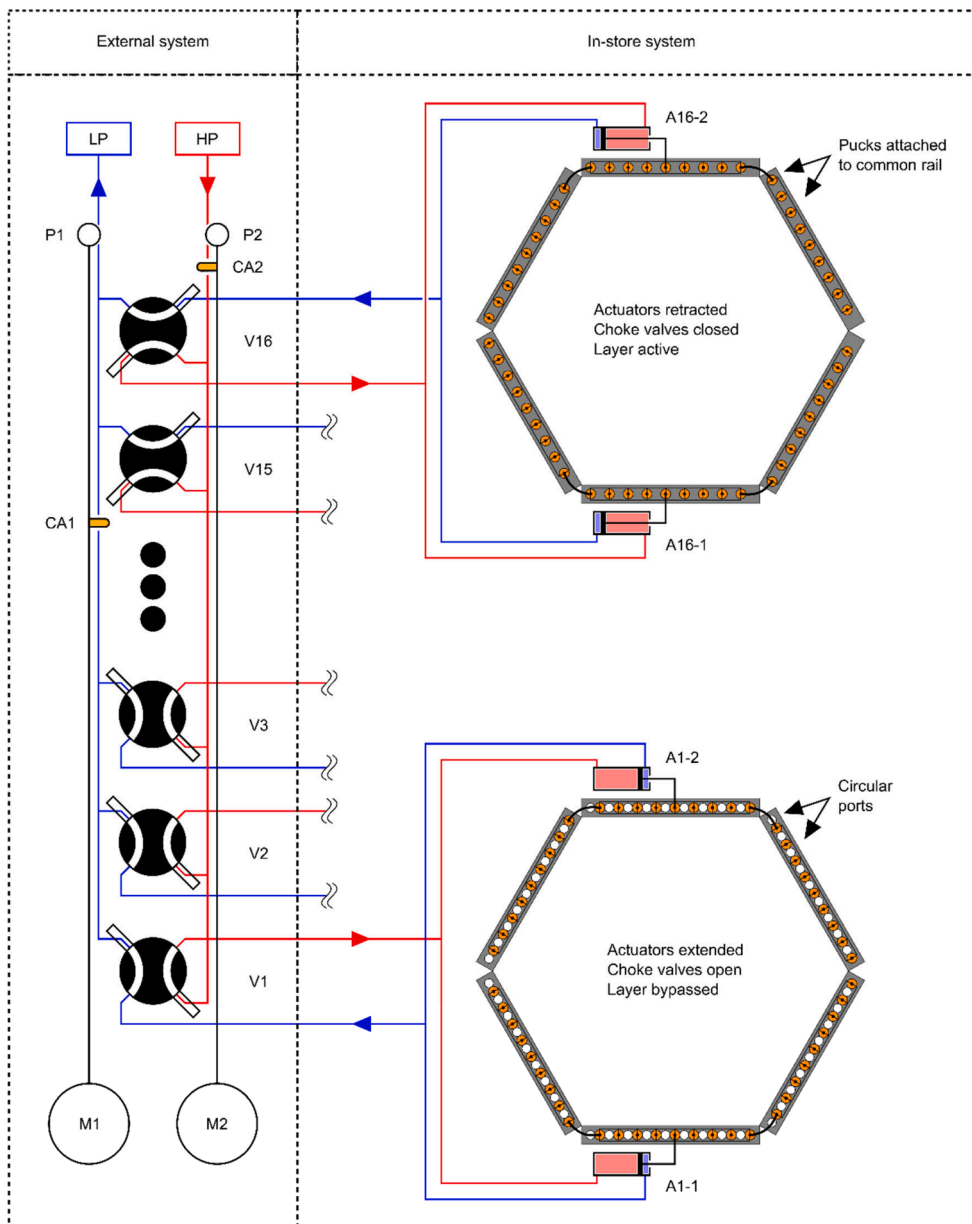
Fig. 4. Basic schematic of Layer Control System hardware. Key: A – Actuator, CA – Carriage arm, LP – Low-pressure supply, HP – High-pressure supply, M – Motor, P – pulley, V – 4-port valve. The internal subsystem shows choke valve mechanism for the top and bottom layers only. The top layer is in charging state as the choke valves are closed and gas cannot be bypassed. The bottom layer is inactive as the choke valves are open and gas is bypassed. The external subsystem shows 4-port valves for the top two and bottom three layers only.

ports (⌀ 50 mm) in the base to cover or uncover them. In this way, each layer receives gas coming through a total of 54 ports in the circumference of the hexagon yielding a uniform flow distribution – refer to Fig. 4 which shows top view of the top and bottom layers (only) with closed and open choke valves, respectively. These choke valves are moved simultaneously by 2 oppositely positioned, double-acting pneumatic actuators such that each actuator shunts 3 adjoining choke valves. The external subsystem consists of a series of (as many as the number of layers) mechanical 4-port valves mounted in parallel onto a carrier frame. These valves pneumatically control the actuators as they can reverse the high- and low-pressure pneumatic supply connections to the in-store actuators, as can be seen in Fig. 4. The pressure differential required by the actuator to work is 3 bar – the high-pressure supply is at hot store operating pressure whereas the low-pressure supply is 3 bar less than the hot store pressure. The 90° movement of the 4-port valves is controlled by a pair of carriage arms, one on each side of the row of 4-port valves. These carriage arms are driven via two motors and timing-belt-pully mechanism, one for each carriage arm. Various micro switches and reed switches are used (not shown in the figure) to signal

the location of the carriage arms and change in the status of the valve in each layer. The external subsystem is contained within a pressure vessel supported by a bracket, which mounts on the store (see Fig. 6b). Fitted outside the store the required high- or low-pressure pneumatic signals to the actuator are sent via 32 pneumatic feed tubes (2 tubes per layer). Through a provision within the layers, a set of these tubes runs along the length and width of the store to feed the pair of actuators on both sides of each layer. The LabVIEW program of the LCS communicates with the Main Control System (MCS) to use the set of temperature readings from the in-store thermocouples to determine when to open or close the choke valves in a particular layer.

The whole choke valve and actuation system for the layer control was designed in-house according to specific principle needs required for proper working of the bespoke layered store. Careful design required appropriate material selection for each component so that it can withstand the high- and -low temperature and pressure of the working gas. Particular focus was given to pneumatic actuators as their failure would significantly affect the storage performance. Safety relief valves were used to protect the actuators against any overpressure. The actuators
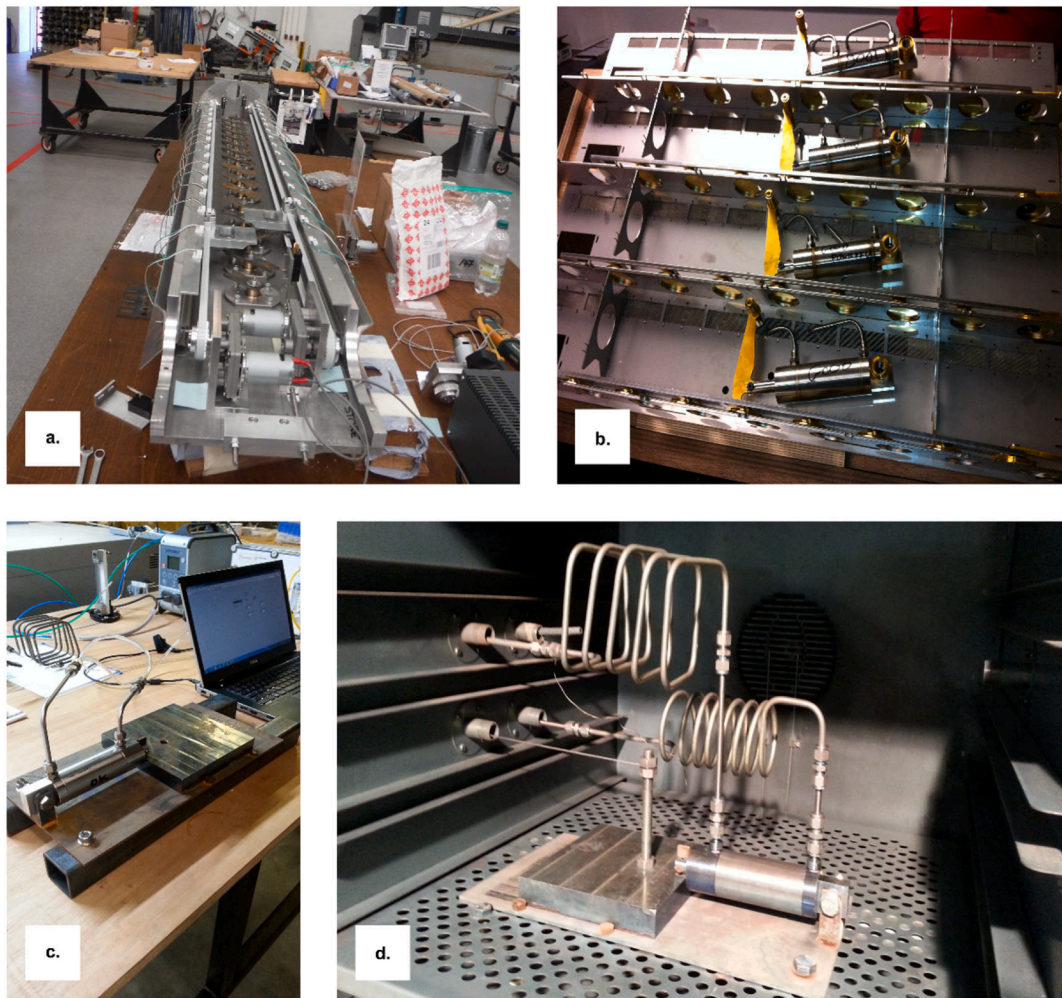
Fig. 5. Layer Control System at fabrication and commissioning stage. **a.** 4-port mechanical valve system, **b.** pneumatic actuators and choke valves attached to a store stack wall, **c.** actuator testing against a load at room temperature, and **d.** actuator testing at 500 °C in oven.

were commissioned prior to their use in the store. The testing mainly involved checking of generation of sufficient force in both directions to operate the choke valves and identification of any significant leaks from the graphite seals and Swagelok gas fittings. On a customised rig, shown in Fig. 5c, the actuator was continually cycled back and forth under required pressure differential at room temperature for a number of cycles. After this, the actuator was oven tested at 500 °C for 600 plus cycles to observe any premature component failure due to thermal expansion and see any potential degradation of the graphite packing seals (see Fig. 5d). The reliability of the choke valves at higher design temperatures was thus ensured prior to hot store performance evaluation in the present study.

Controlling the layers in a specific way governs the shape of thermocline. As stated previously, a narrower thermocline is required for a number of reasons, one of which is the better utilisation of the store. This is achieved by programming the LCS such that in view of the received store thermocouple data when specific temperature criteria is fulfilled only pertinent layers are activated and deactivated during charge and discharge. The same strategy is applied to the model to generate numerical results. It is noteworthy that during charge, the top layer charges first and the thermal front slowly moves down to the bottom layer. The thermal front moves in the reverse direction during discharge.

Consider that T_c and T_d are the charge and discharge temperatures respectively, and ΔT is their difference. During charge, the next layers at the leading edge of the front are activated when the temperature difference between the (rising) temperature of the gas exiting the layer

forming the nose of the front and the discharge temperature exceeds 8.5 % of the overall required temperature rise *i.e.,* $(T_g - T_d) > 0.085 \times \Delta T$. Similarly, the previous layers at the trailing edge of the front are deactivated when the temperature difference between the (rising) temperature of the gas exiting the layer forming the tail of the front and the discharge temperature exceeds 91.5 % of the overall required temperature rise *i.e.,* $(T_g - T_d) > 0.915 \times \Delta T$. The same approach is implemented during discharge, but with the conditions for nose and tail replaced and inequality symbols reversed.

2.3. Experimental test setup

A basic schematic of the experimental setup and photograph are shown in Fig. 6. Mainly, the setup consists of a fan, heater and the store.

A radial type blower fan, connected at the bottom of the store, was used to circulate atmospheric air used as the HTF at near ambient pressure. The fan was directly connected to a 37 kW variable speed drive motor to vary air mass flow rate depending upon the store pressure drop. A 108 kW electric heater was connected to the top of the store. During charge, the heater heats the air to the required working temperature (≈131-146 °C) which then enters the store from the top and leaves after transferring its heat to the storage media at near ambient temperature from the bottom. During discharge, the ambient air enters from the bottom and leaves after receiving the heat from the storage media from the top whilst the heater is kept switched off. Pipeline connections and several manually operated valves between the fan and store enable flow
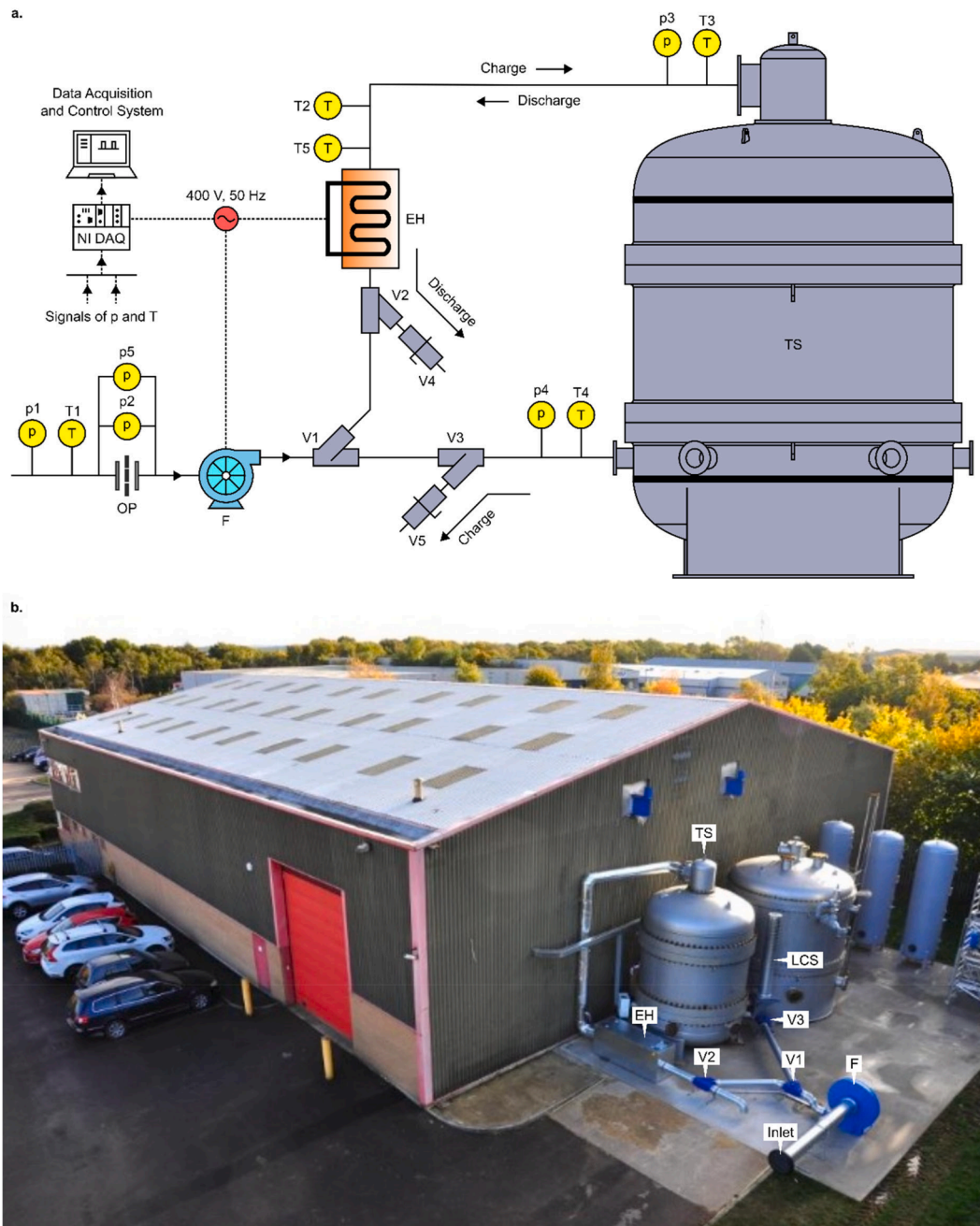
Fig. 6. **a.** Basic schematic of the external experimental setup. Key: EH – Electric Heater, F – Fan, OP – Orifice Plate, P – Pressure Sensor, T – Temperature Sensor, TS – Thermal Store, V – Valve. Note: The duct between EH and the store top is externally insulated using 50 mm thick rockwool layer, and **b.** A photograph of the hot TS with the testing equipment. The store was built and tested in Hampshire, UK.

reversal during these charge/discharge periods, as indicated in Fig. 6(a & b). Diverter valves (V1, V2 and V3) cause the changeover between charge and discharge periods whereas damper valves (V4 and V5) fitted downstream of the two outlet diverter valves allow the system back pressure and mass flow rate to be adjusted. An orifice plate was placed at the inlet duct before the fan to calculate the air mass flow rate. The orifice plate was sized to give a differential pressure of 3 kPa at the design mass flow rate of 0.7 kg/s.

2.4. Instrumentation and data logging

Local gas and solid temperatures inside the store were measured using *N*-Type thermocouples, along the axial direction only, as shown in Fig. 7a. Sixteen thermocouples were placed in the middle of each layer

to record the solid temperature. Fifteen thermocouples were suspended in the voids above the storage media between each layer to record the gas temperature. Two additional thermocouples were placed for recording the gas temperature with one placed above the top layer and one below the bottom layer. All these thermocouples were fitted on one of the vertical posts at the respective layers by using brackets, at a distance of one-third of the store radius from the centre. Fig. 6a shows various thermocouples and pressure sensors fitted around the external circuit (outside the store). All the pressure sensors were calibrated prior to their use. Absolute pressure, *p1*, ambient temperature, *T1*, and the differential pressure, *p2*, across the orifice plate allow the air mass flow rate to be determined. One thermocouple measures the air temperature, *T2*, downstream of the heater. Two pressure sensors, *p3* and *p4*, and two thermocouples, *T3* and *T4*, are fitted to the top and bottom ducts to
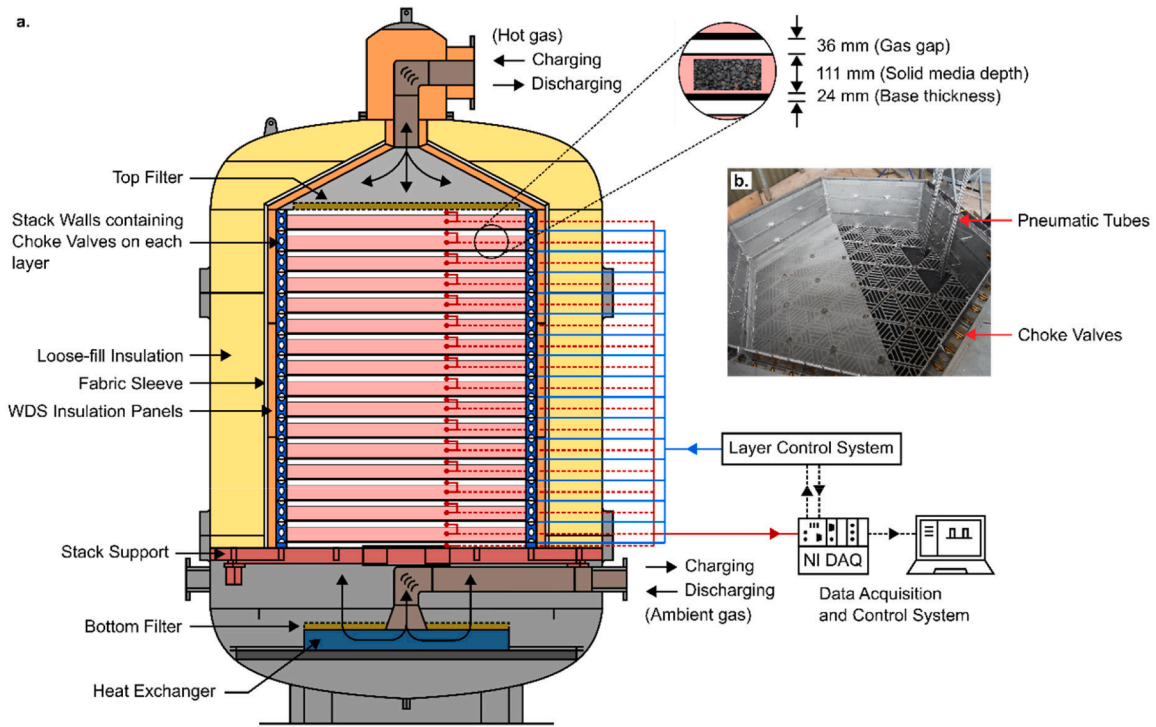
Fig. 7. a. TS section showing principal features (not to scale). In-store thermocouples are shown with red dots. Thermocouples in the gas gaps are numbered 0 to 16 from bottom to top whereas those in the layers are numbered 1 to 16. LCS receives thermocouple data from the MCS (red dotted lines) and sends pneumatic signals (blue lines) to the valves to activate/deactivate the layers, and **b.** A photograph of one layer of the store during construction. The storage media is poured on top of the mesh and supported by a lightweight structure. Choke valves in one side wall of the stack in closed position can also be seen. (For interpretation of the references to colour in this figure legend, the reader is referred to the web version of this article.)

Table 2
Testing equipment and instrumentation details.

Component	Acquired from	Details	
Fan	Halifax Fan	37 kW, 2950 rpm, $\dot{m}_{g,\ design}$ = 0.7 kg/s	
Electric heater	Neatafan ltd	108 kW, connected with thyristor controller	
Orifice Plate	–	⌀ 131.6 mm, p1 – p2 = 3 kPa at 0.7 kg/s	
Sensor type and name	Acquired from	Range	Accuracy
N-Type in-store thermocouples	TC ltd	0 to + 1100 °C	± 1.5 °C (−40 to + 375 °C)
			± 0.004 T °C (+375 to + 1000 °C)
T-type external thermocouples, T1 – T4	TC ltd	−185 to + 300 °C	± 0.5 °C (−40 to + 125 °C)
			± 0.004 × T (+125 to + 350 °C)
Pt-100 temperature sensor, T5	Neatafan ltd	−100 to + 450 °C	± 0.3 + 0.005 × T
Pressure sensors (abs), p1, p3, p4	RS Components	0 – 200 kPa	± 0.1 % V$_{FS}$ (38.5 – 41.5 mV)
Differential pressure sensor, p2	Siemens	0 – 3 kPa	< ± 3 % V$_{FS}$ (DC 0 – 10 V)
Differential pressure switch, p5	Neatafan ltd	0.02 – 0.3 kPa	± 0.0025 kPa (repeatability)

measure the air pressure (abs) and temperature, respectively.

Besides LCS described in *Sec*. 2.2, two more control systems were employed. The Fan Control System (FCS) controls the fan speed to maintain a constant mass flow rate. The FCS also starts and stops the heater when required. The Heater Control System (HCS) is a programmable temperature controller and is responsible for maintaining a specific heating profile for the gas at the store inlet during charge, using feedback from temperature sensor, *T5*. The pressure switch, *p5*, provides confirmation of air flow and is interfaced directly to the HCS. All of the sensor data was recorded and logged using National Instruments I/O modules and a Graphical User Interface (GUI) was developed using LabVIEW software for this purpose. All in-store thermocouple data was logged by the MCS every 10 s whereas the external data *i.e.,* fan speed, temperatures, *T1* to *T4*, and pressures, *p1* to *p4*, were logged every 5 s using a separate (but time-synchronised) store test logging system. Details of the rig components and instrumentation are summarised in Table 2.

3. Fluid dynamic and heat transfer model for numerical analysis

To design an efficient ES system and further investigate its thermodynamic aspects, it is important to carefully understand the thermocline behaviour of the packed-bed. For this purpose, most of the prior studies use the 'flow through porous media' approach, and are supported by the well-known 1-dimensional, 2-phase (2-equation) formulation presented by Schumann [76]; this includes one equation each for the gas and solid phases suggesting that $T_g \neq T_s$ at any local position, and that the properties of gas and solid vary only along the direction of the gas flow. This approach has been widely recognised as a building block for research on this topic, and is practiced in the present work.

3.1. Model assumptions

A few assumptions have been considered. It is noteworthy that these assumptions are meant to make the 'gas-solid' model thermally simple (of course without compromising the reliability of results) and are reasonably justified, as will be shown later through the comparison of experimental and model results. The assumptions are:

1. Thermal resistance inside the solid particles compared to the exterior surface is negligible ($Bi \ll 1$): this eliminates the need to model a complex temperature field inside the particles

2. Heat transfer is dominated by convection: heat transfer by conduction within the gas and the particles themselves has a minor effect, as has been reported previously [74,77]. Moreover, the current testing does not involve an 'idle storage phase' between charge and discharge where conduction may play a role. Radiative heat transfer is also ignored as the experiments were conducted at a lower temperature

3. Store side walls are adiabatic: this being due to adequate insulation available around the store

4. No heat loss takes place through the 'gas gaps' between and around successive layers *i.e.,* the temperatures of both the gas and solid at the axial ends of two successive solid media layers and therebetween is uniform: this allows the model to consider only the 'effective' length of the store, made up by individual depths of solid media layers

5. Storage material is evenly distributed: porosity is constant in any direction, especially near the wall *i.e.,* no flow channelling is present. This assumption is further supported by the fact that the store in the present investigation has considerably large equivalent diameter than the mean particle diameter ($D > d_p$) such that this effect is negligible

6. The store is of circular cross-section: an equivalent diameter is used for the numerical analysis (see Table 1).

3.2. Governing equations

Considering these assumptions, we can write equations governing the pressure and temperature variation through the store. Firstly, an equation is presented to represent heat transfer rate, δQ, for the gas–solid network for a segregated, arbitrary control volume of the store, shown in Fig. 8.

$$\delta \dot{Q} = h \delta A (T_g - T_s) \qquad (1)$$

where $h = Nuk_g/d_p$ is the convective heat transfer coefficient, $\delta A = A \delta z (1 - \varepsilon)S_v$ is the differential heat transfer surface area in which $\varepsilon = V_g/V$ is the void fraction, or store porosity, and $S_v = 6/d_p$ is the particle surface area-to-volume ratio. As suggested in [77], for the involved range of Reynolds number, the convective heat transfer coefficient is estimated using Nusselt number correlation taken from [78], as in the following equation.

$$Nu = 2.0 + 1.10Pr^{1/3}Re_p^{3/5}; \left(15 < Re_p < 8500\right) \qquad (2)$$

where $Re_p = Gd_p/\mu_g$ is the particle Reynolds number.

For the same control volume, we can write mass balance, momentum balance and energy balance for the gas phase and energy balance for the solid phase, in the form of partial differential equations, (3)-(6),
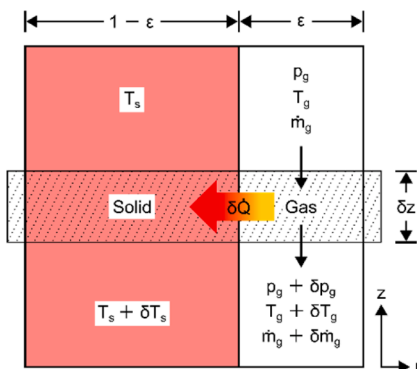

Fig. 8. Arbitrary gas–solid system control volume.

respectively [36,74], as follows:

$$\text{Mass :} \quad \varepsilon \frac{\partial \rho_g}{\partial t} + \frac{\partial G}{\partial z} = 0 \qquad (3)$$

$$\text{Momentum :} \quad \varepsilon \frac{\partial G}{\partial t} + \frac{\partial}{\partial z} \left(\frac{G^2}{\rho_g} + \varepsilon^2 \left(p - \rho_g gz \right) \right) = -\varepsilon(1 - \varepsilon)S_v \tau_s \qquad (4)$$

$$\text{Energy (gas) :} \quad Gc_p \frac{\partial T_g}{\partial z} + \varepsilon \left(\rho_g c_p \frac{\partial T_g}{\partial t} - \frac{\partial p}{\partial t} \right) = -\frac{\delta \dot{Q}}{\delta V} \qquad (5)$$

$$\text{Energy (solid) :} \quad \delta m_s c_s \frac{\partial T_s}{\partial t} = \delta \dot{Q} \qquad (6)$$

In the above equations, G is the mass flux, given as $G = \rho_g U_o = \dot{m}_g/A$ where U_o is the empty-column gas velocity (related to the interstitial gas velocity as $U_o = \varepsilon U$). c_p and c_s are the gas and solid specific heat capacities, respectively. τ_s is the shear stress on the solid particles.

The gas dynamics and thermal response of the store are thus captured numerically by integrating Eqs. (3)-(6) with respect to *space* and *time* variables in a coupled fashion. Changes in density are usually small when temperature changes are not big and, therefore, on most occasions have been ignored to simplify the analysis [74,77]. Here, however, these are taken into account using Eq. (3) for precisely evaluating the thermocline behaviour. Changes in pressure (and hence the store pressure drop) are calculated using Eq. (4). Eqs. (5) and (6) are solved to compute temperature variation of the gas and solid.

Under given conditions of gas flow in a typical case like this, the dynamic and hydrostatic pressures vary negligibly along the store and viscous effects dominate the velocity driven inertial effects. Ignoring the unsteady gas term leaves Eq. (4) in a simplified form to give pressure drop through the store, as given in Eq. (7).

$$\frac{\partial p}{\partial z} = -\frac{G^2(1 - \varepsilon)S_v f}{\varepsilon^3 \rho_g}; f = \frac{5}{Re_m} + \frac{0.4}{Re_m^{0.1}} \qquad (7)$$

where f is the friction coefficient, which according to the modified Reynolds number, $Re_m = G/(1 - \varepsilon)S_v\mu_g$, has a turbulent flow regime ($Re_m > 2.0$) and is given by the Carman correlation [79].

The energy equations can also be reorganised, as below, by incorporating three variables to assist in numerical integration [36,74]:

$$\frac{\partial T_g}{\partial z} = -\frac{T_g - T_s}{l} + F; l = \frac{Gc_p}{h(1 - \varepsilon)Sv}; F = \frac{\varepsilon}{Gc_p} \left(\frac{\partial p}{\partial t} - \rho_g c_p \frac{\partial T_g}{\partial t} \right) \qquad (8)$$

$$\frac{\partial T_s}{\partial t} = \frac{T_g - T_s}{\tau}; \tau = \frac{\rho_s c_s}{hS_v} \qquad (9)$$

where l and τ are the length and time scales, respectively, and F accounts for unsteady accumulation of the gas. The numerical integration algorithm used to solve Eqs. (3), (7), (8) and (9) is essentially based on the latest approach devised in [74,77], and for completeness is provided below (with similar notation for consistency). It should be noted that this numerical approach has not been verified before against any experimental data.

3.3. Numerical integration

The numerical method used here employs a semi-analytical approach the significance of which was demonstrated theoretically by White [77] (and used in their later papers) in terms of improved computational efficiency and numerical stability along with the allowance of larger space and time steps. Fig. 9 illustrates a three-step section of the space–time computational grid marked with nodes. To evaluate the unknown gas and solid temperatures at a current node (i,n), temperatures are known at each node for the previous time step, $n-1$, and at nodes up to and including the previous space step, $i-1$, for current time step, n. This follows with analytical integration of Eq. (8) between space

steps, $i – 1$ and i at current time step, n, whilst keeping T_s and F constant at their average values, as given in Eq. (10).

$$T_{g,i,n} = (1-a)\overline{T}_s + aT_{g,i-1,n} + (1-a)\overline{F}l \tag{10}$$

Likewise, Eq. (9) is integrated between time steps, $n – 1$ and n at current space step, i, whilst keeping T_g at its average value, as shown in Eq. (11).

$$T_{s,i,n} = (1-b)\overline{T}_g + bT_{s,i,n-1} \tag{11}$$

where $a = e^{-\Delta\xi}$ and $b = e^{-\Delta\eta}$ in which $\Delta\xi = \Delta z/l$ and $\Delta\eta = \Delta t/\tau$ are the dimensionless length and time variable differences. The average temperatures are:

$$\overline{T}_g = \frac{T_{g,i,n-1} + T_{g,i,n}}{2}; \quad \overline{T}_s = \frac{T_{s,i-1,n} + T_{s,i,n}}{2}$$

The average value of F to be used in Eqs. (10) and (11) is determined using the already-known values at nodes, $(i – 1, n – 1)$ and $(i – 1, n)$.

$$\overline{F} = \frac{\varepsilon}{Gc_p}\frac{1}{\Delta t}\left(\left(p_{i-1,n} - p_{i-1,n-1}\right) - \overline{\rho}_g c_p\left(T_{g,i-1,n} - T_{g,i-1,n-1}\right)\right)$$

Eq. (7) is then used to compute pressure drop between each node in a straightforward finite-difference manner. New gas property values can be used to obtain gas density at the current space and time step, which finally allows updating of the mass flux using Eq. (12) below:

$$G_{i,n} = G_{i-1,n} + \varepsilon\frac{\Delta z}{\Delta t}\left(\rho_{g,i,n-1} - \rho_{g,i,n}\right) \tag{12}$$

3.4. Specific heat capacity of storage media

The variation in specific heat capacity of the storage media with temperature leads to considerable changes in the model results. The specific heat capacity of the storage media, c_s, consisting of bulk magnetite with a small fraction of silica, was calculated using the expression:

$$c_s = \frac{(\rho_s - \rho_{sil}) \times \rho_{mag}c_{mag} + (\rho_{mag} - \rho_s) \times \rho_{sil}c_{sil}}{(\rho_{mag} - \rho_{sil}) \times \rho_s} \tag{13}$$

where ρ_s and ρ_{mag} are the bulk density of the solid media and the density of pure magnetite respectively. (Their values are given in Table 1). The density of pure silica, ρ_{sil}, is 2650 kg/m³. The specific heat capacities of pure magnetite, c_{mag}, and silica, c_{sil}, varies with the temperature and, therefore, temperature-dependent property data was used in the numerical analysis to predict the results accurately. The property data for both the magnetite and silica were taken from [80,81] and [82] respectively. Subsequently, a curve fitting procedure was applied in Excel® to evaluate c_{mag} and c_{sil}, both in J/kg K. The resulting functions in terms of the unknown solid temperature, T_s (K), were used in the numerical integration scheme. These are presented below:
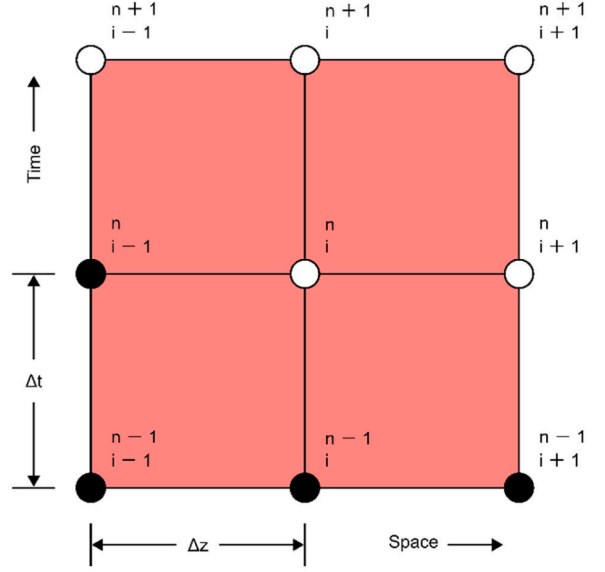

Fig. 9. Space-Time computational mesh.

$$c_{sil}(T_s) = 445.9\ln T_s - 1777.4 \tag{15}$$

It is noteworthy that magnetite undergoes a transition phase at about 120 K presumably due to changes in the magnetic properties. This behavior was included in the curve fitting procedure and is represented by the second condition in Eq. (14).

4. Model validation and discussion of experimental results

Firstly, the numerical model is validated against the experimental data to ensure that the model is sufficiently accurate, and the assumptions presented in *Sec.* 3 are reasonably justified. In the study the performance of *layered* TS against its *simple* counterpart has been evaluated by operating the same store in two modes: simple and layered. In the simple mode the LCS remains completely inactive such that the gas bypass choke valves remain closed during operation. On the contrary, in the layered mode the store is operated with the LCS remaining completely functional allowing for a controlled flow path for the gas. From here on, for simplicity, the store operation will be regarded as 'simple mode' and 'layered mode'.

4.1. Experimental conditions

In the simple mode the store was operated at conditions: $T_c = 131\,°C$, $T_d = 23\,°C$, $\dot{m}_g = 0.4$ kg/s. In the layered mode the store was operated at slightly different conditions: $T_c = 146\,°C$, $T_d = 26\,°C$, $\dot{m}_g = 0.5$ kg/s. The

$$c_{mag}(T_s) = \begin{cases} 375.0\ln T_s - 1485.0 + \dfrac{568.0(T_s - 111.0)}{8.0}, 111.0 < T_s \leq 119.0 \\[2mm] 375.0\ln T_s - 1485.0 + \dfrac{568.0(120.5 - T_s)}{1.5}, 119.0 < T_s \leq 120.5 \\[2mm] 375.0\ln T_s - 1485.0, 120.5 < T_s \leq 365.0 \\[2mm] -6.30 \times 10^3 + 6.33 \times 10^1 T_s - 2.29 \times 10^{-1}T_s^2 + 4.16 \times 10^{-4}T_s^3 - 3.75 \times 10^{-7}T_s^4 + 1.35 \times 10^{-10}T_s^5, \\[1mm] 365.0 < T_s \leq 840.0 \end{cases} \tag{14}$$

Table 3
Experimental conditions for the two demonstration runs using air as HTF.

Mode	Parameter	Charge	Discharge
Simple	$\dot{m}_g$ [kg.s^{-1}]	0.4	0.4
	G [kg.s^{-1}.m^{-2}]	144×10^{-3}	144×10^{-3}
	p [bar]	1.01	1.01
	T [°C]	131	23
	T_{amb} [°C]	17	18.5
	$T_{g,s,\ init}$ [°C]	17	Same as end of charge
	t [hr]	5.40	5.40
Layered	$\dot{m}_g$ [kg.s^{-1}]	0.5	0.5
	G [kg.s^{-1}.m^{-2}]	180×10^{-3}	180×10^{-3}
	p [bar]	1.01	1.01
	T [°C]	146	26
	T_{amb} [°C]	13	21
	$T_{g,s,\ init}$ [°C]	14	Same as end of charge
	t [hr]	4.55	4.55

experimental conditions, charge temperature and flow rate in particular, were not met in the two cases due to some technical difficulties faced during these experiments – the main reason being the gas leaking past a layer during the layered mode operation. Nevertheless, irrespective of the minor leakage (as indicated by the two deviating data points on the "80 min" curve in the Fig. 12c), it was possible to retrieve a full set of data for each mode at the conditions stated above. The pressure was kept nearly constant at ~ 1 bar throughout for both modes. As the two experiments were not conducted on the same day, the ambient conditions slightly varied which resulted in different discharge temperatures as well as the initial store temperature prior to charge. The ambient temperature also varied significantly between charge and discharge during the layered mode operation compared with a nearly uniform value during the simple mode operation. Furthermore, the air received at the store bottom during discharge for both experiments was at ~5 °C higher temperature than the corresponding ambient temperature; this being due to the kinetic energy imparted to the air by the blower. A summary of the experimental conditions is given in Table 3.
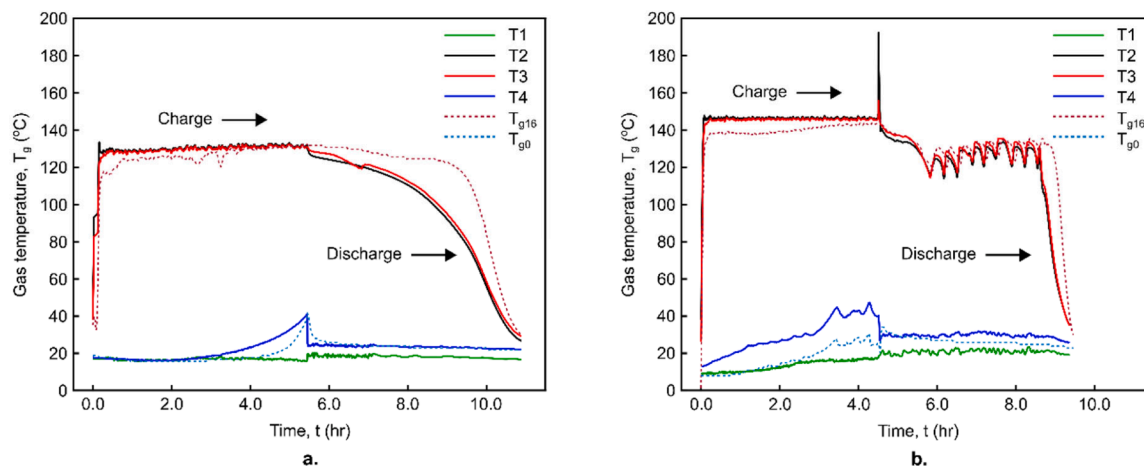
4.2. Temperature curves

Fig. 10 shows the experimentally measured curves at various points around the setup highlighting the store inlet and exit temperatures for the two modes for a complete cycle. Importantly, compared with the simple mode, in case of layered mode, the discharge temperature

remains nearly uniform (around its mean value) for a longer time as desired, thereby demonstrating the practical advantage of using a multi-layered store. However, due to minor gas leakage past the closed valves observed during the layered operation (Fig. 12c), the discharge temperature initially drops sharply to 115 °C and once the thermal front has crossed the leaking layer, it gradually regains its final (maximum) value of 134 °C towards the end. The wavy pattern of the discharge temperature is specifically because of the LCS.

Figs. 11 and 12 show the experimental gas and solid temperature profiles plotted against the model results for the two cases for a complete cycle. For the simple mode, the temperature profiles are shown on Fig. 11, drawn every 45 min except for the last one which is 54 min later marking the end of charge and start of discharge. Similarly, for the layered mode, the temperature profiles are shown on Fig. 12, drawn every 40 min except for the last one which is 33 min later marking the corresponding end of charge and start of discharge. In practice, the charge and discharge phases are concluded when specific temperature criteria are met (Sec. 2.2). For gas, the experimental data is represented by curves drawn using 17 data points (via thermocouples in the gas gaps). Likewise, for solid, the experimental data is represented by curves drawn using 16 data points (via thermocouples in the solid layers). It should be noted that for use in the numerical model the initial conditions at the beginning of charge are kept the same as the experimental conditions recorded at "0 min" which are nearly ambient (Table 3). However, at the beginning of respective discharge phase the corresponding initial conditions for the model are not the same as the experimental conditions at the end of charge phase. Instead, the initial conditions for the model are the same as that at the end of the charge phase achieved through the model. As will be discussed shortly, this is because of slight deviation in the model results from the experimental data towards the end of charge.

As can be seen from Figs. 11 and 12, the model results generally agree very well with the measured experimental data. The thermal front movement is accurately predicted in line with the experimental data. During charge, on a dimensionless length scale of 0.0–1.0 (store top to bottom), this prediction is particularly accurate up to ~0.7 which forms most part of the store length. Beyond this point up to the bottom end of the store a slight gradually increasing deviation is observed as the simulated thermal fronts seem to remain sharper (as before) compared with the experimental data. The same behaviour is observed during discharge. It is noteworthy that since there is no *storage* phase between the *charge* and *discharge* phases *i.e.,* the discharge phase follows quickly

Fig. 10. Gas temperature curves as measured by the four external, *T1 – T4* (solid lines), and two instore, T_{g16} and T_{g0} (dashed lines), gas thermocouples. **a.** simple mode operation, and **b.** layered mode operation. The data was smoothed before plotting. Temperatures measured by the thermocouples *T2* and *T3* indicate negligible duct heat losses as this section of the external setup was well insulated. However, the instore thermocouples at the top and bottom, T_{g16} and T_{g0}, show some differences with their nearest external thermocouple, *T3* and *T4*, values respectively, partly because of associated combined inaccuracy of ± 2 °C. The difference between T_{g16} and *T3* is the highest in case of simple mode discharge period which might be because of relatively lower mass flux in addition to the thermocouple inaccuracy.
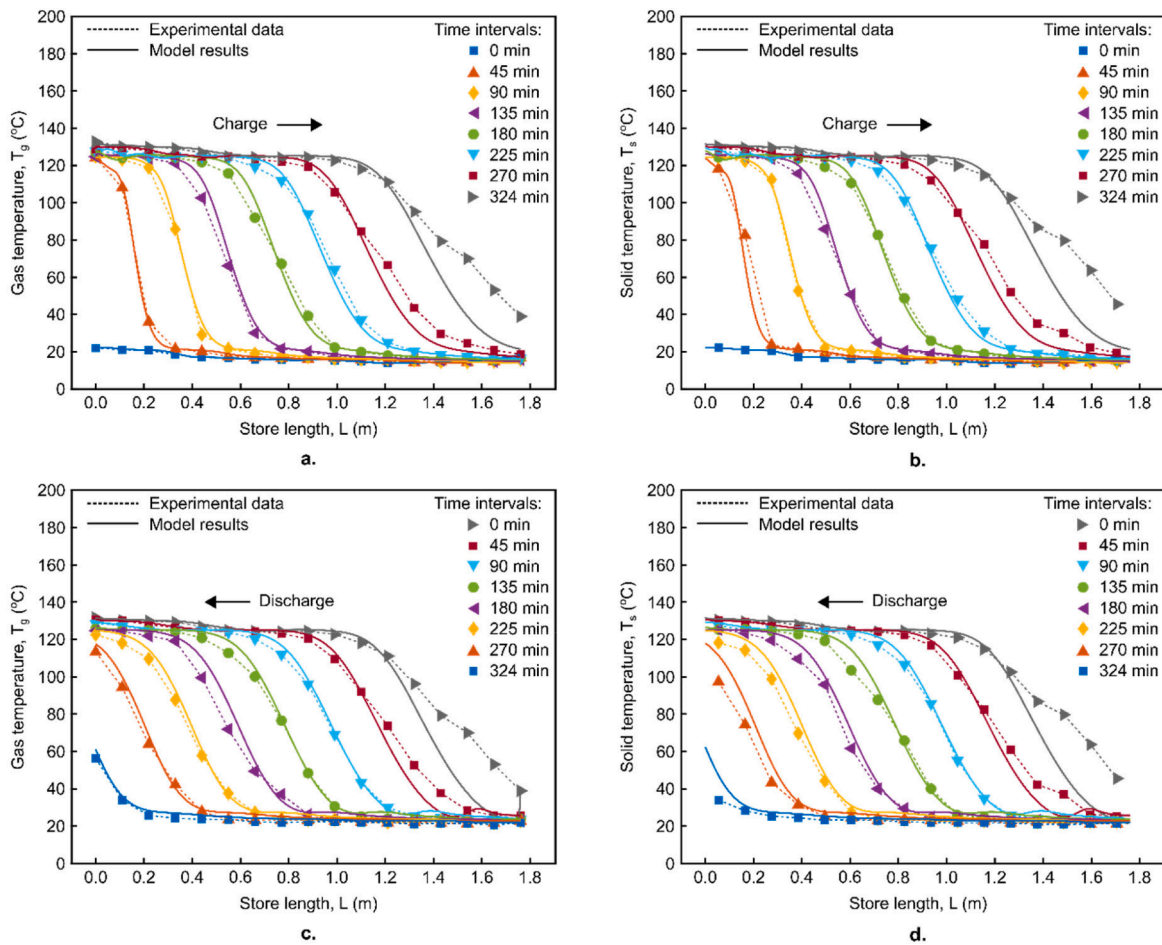
Fig. 11. Experimental data (points marked on dashed lines) plotted against model results (solid lines) showing temperature profiles of the store in simple mode operation at $T_c = 131$ °C and $\dot{m}_g = 0.4$ kg/s. **a.** gas profiles during charge, **b.** solid profiles during charge, **c.** gas profiles during discharge, and **d.** solid profiles during discharge.

after charge phase ends in the experiments, there is no considerable heat loss and ideally the initial conditions at the onset of the discharge should remain the same as those at the end of the charge: this holding true for both the experimental and model results. However, due to the increasing deviation between the experimental and model results towards the end of charge, the initial conditions for the modelling of discharge phase cannot be kept same as this would eventually lead to misleading temperature profiles resulting in an earlier completion of the discharge. As shown in Fig. 11(c & d) and Fig. 12(c & d), during discharge, this situation ultimately leads to the thermal front behaviours as if they are similar but just in reverse *i.e.,* from bottom to top, first yielding maximum deviation then gradually reducing to eventually match the curves towards the end of discharge. Overall, this deviating behaviour near the store bottom is due to the gradual build-up of heat in the store over the duration of the charge phase – a phenomenon not captured by the model.

4.3. Pressure curves

Pressure across the store was measured only at two locations: top and bottom. Fig. 13 shows the comparison of pressure variation in the two operational modes. The generally increasing pressure during charge and decreasing pressure during discharge is because of the changing ambient conditions on the day of the experiments. For charge, the average recorded inlet pressure for both experiments was ~1.024×10^5 Pa whilst for discharge, this value was higher for the layered mode (1.047×10^5 Pa) than the simple mode (1.031×10^5 Pa). The numerical model

uses the measured inlet values of the pressure during the whole cycle. As can be seen from Fig. 13, the outlet pressure, and hence the resulting pressure drop, is accurately predicted by the model to a good degree. Although the working conditions are slightly different for the two modes but clearly the store pressure drop can be observed to be noticeably reduced in the layered mode than the simple mode. An average pressure drop of 1.95 kPa for one complete cycle is observed for the simple mode as compared with a corresponding value of 0.7 kPa for the layered mode, indicating ~64 % reduction.

5. Comparison of performance at design conditions

It is necessary to predict the hot TS performance at its actual operating conditions for use as part of the 150 kW$_e$, 600 kWh$_e$ PHES demonstrator operating at full load. Therefore, having gained confidence from the validated model, additional simulations were run for a meaningful comparison between its simple and layered mode operation at same conditions. The conditions are presented in Table 4.

Besides design parameters the storage performance is dependent on two operational parameters: cycle durations and mode of operation *i.e.,* one-off or cyclic operation. We have considered both parameters here. In reality, it may not be possible for the store to charge and discharge completely in respective nominal times, t_N, and so a time control must be implemented. In the layered mode, the charge and discharge periods are set to terminate simply according to the front control strategy (*Sec.* 2.2). In simple mode two scenarios have been considered. In scenario 1, the cycle is stopped when the gas exit temperature reaches a certain value,
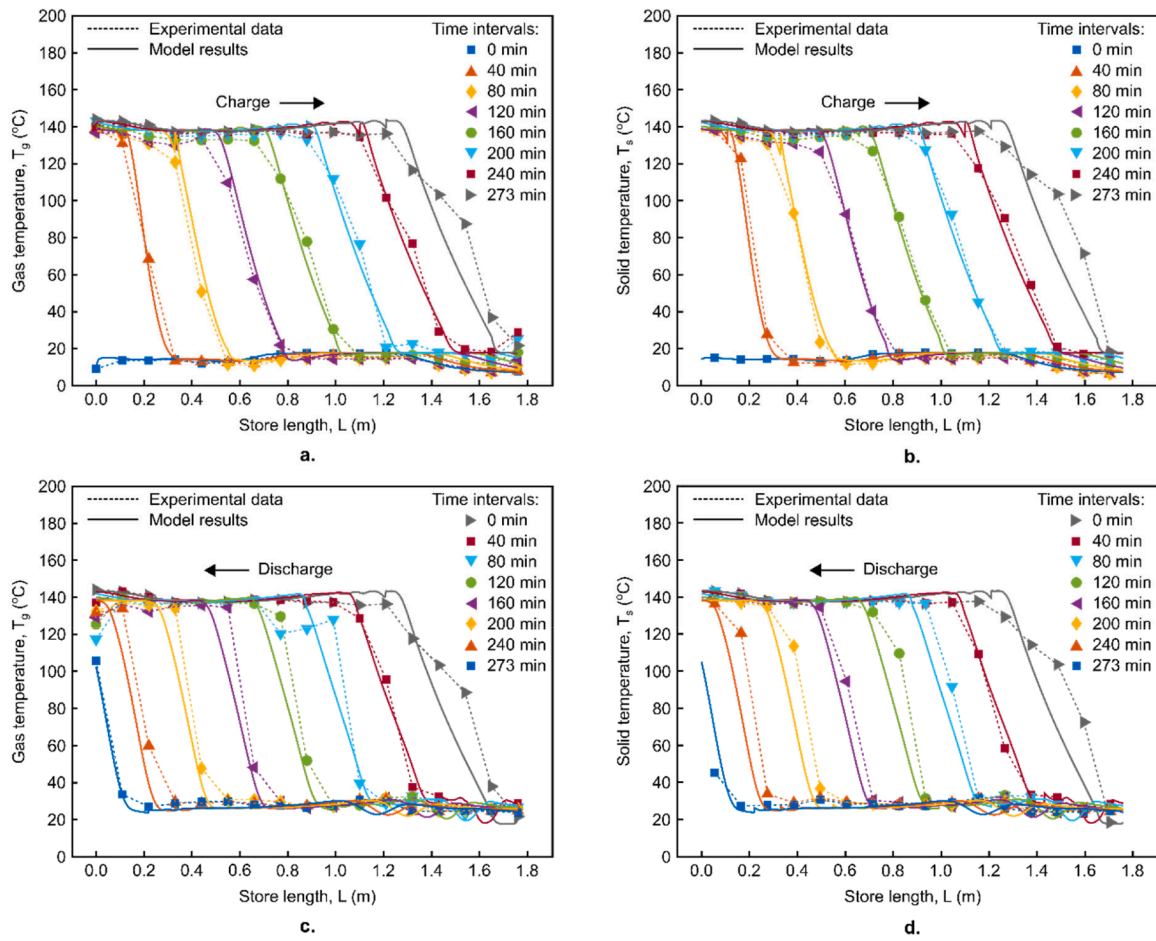
Fig. 12. Experimental data (points marked on dashed lines) plotted against model results (solid lines) showing temperature profiles of the store in layered mode operation at $T_c = 146$ °C and $\dot{m}_g = 0.5$ kg/s. **a.** gas profiles during charge, **b.** solid profiles during charge, **c.** gas profiles during discharge, and **d.** solid profiles during discharge.
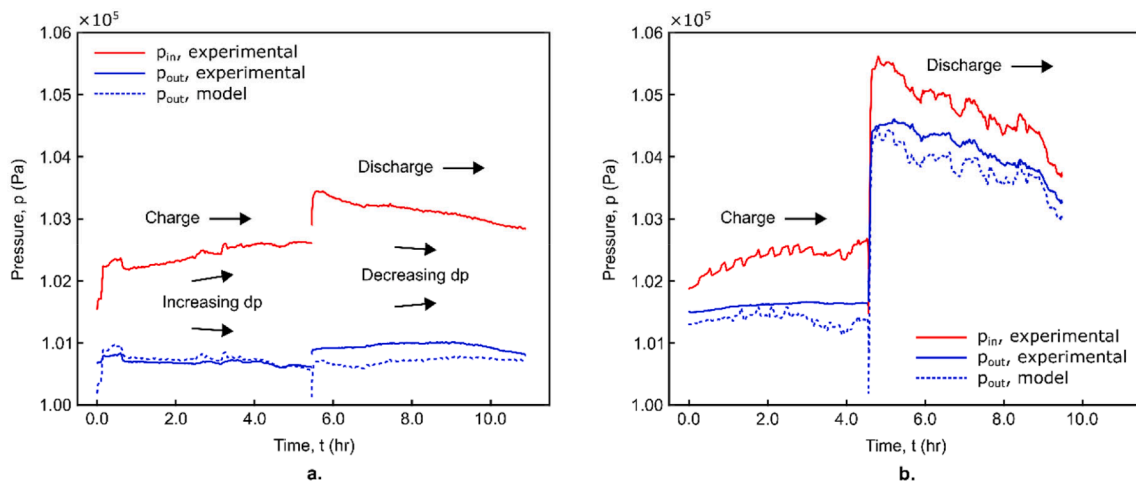

Fig. 13. Pressure variation with time through the stores. **a.** simple mode, and **b.** layered mode.

however, in case of the layered store, next layer will be activated until the final layer has reached. In scenario 2, the charge and discharge durations for the simple mode have been kept same as the final charge and discharge durations of the layered store. Scenarios 1 and 2 are for the simple mode only and can thus be distinguished as having 'temperature-based' and 'time-based' cycle control respectively. Note that

the charge and discharge periods may not be equal to each other in any scenario and in any mode of operation. A TS can be studied based on a number of inter-related performance indicators, such as: thermal front shape, storage process efficiency, energy storage density and utilisation. These key performance indicators have been considered while analysing results from the numerical study presented below.

Table 4
Operating conditions using argon as the HTF.

Parameter	Charge	Discharge
$\dot{m}_g$ [kg.s^{-1}]	1.22	1.22
p [bar]	12	12
T [°C]	500	26
T_{amb} [°C]	26	26
t_N [hr]	4	

5.1. Thermal front behaviour and cyclic operation

As shown in Fig. 14, the layered mode generates narrower and rather steep thermal fronts relative to simple mode. Particular to note is that the prominent wave-like pattern of the thermal front in layered mode is due to front control strategy resulting in steepening of the front and shrinking of the thermocline region. This is one of the main reasons behind layered formation. This eventually leads to increased amount of energy stored and recovered in case of layered mode compared with simple mode in scenario 1. In 1st cycle, layered mode charges in 3.06 hr and discharges in 2.87 hr whereas for simple mode these durations are 2.81 hr and 2.47 hr respectively in scenario 1; simple mode has same durations in scenario 2 as those in the layered mode. The early end of charge and discharge for simple mode in scenario 1 results in the thermal fronts remaining behind compared to scenario 2 because of less time. This pattern is more noticeable and pronounced in cyclic operation where the thermal fronts gradually become wider and longer.

In cyclic operation, temperature profiles tend to become identical gradually between successive cycles leading to a steady-state after an initial transient state. Layered mode converges faster taking only 3 cycles. However, simple mode consumes about 20 cycles in scenario 1 and 5 cycles in scenario 2 to converge. After convergence t_c and t_d also become identical in both modes. Simple mode converges quicker in time-based cycle control in comparison to temperature-based cycle control. However, this would be at the expense of increased exit losses, as will be discussed later. In a situation of simple mode where the cycle is stopped when the exit gas temperature reaches a certain threshold value, with each passing cycle the elongation of thermal front results in curtailment of durations (($t_c = t_d = 1.68$ hr after convergence). Fig. 14 shows that for layered mode there is not much difference in thermal fronts shape in the first and last, steady state cycles.

5.2. Effect of layering on pressure drop

Fig. 15 shows comparison of pressure at store inlet and exit between layered mode and simple mode of scenario 2 for 1st cycle. As expected,

layered mode results in reduced pressure drop comparatively; the computed pressure drop reduction is ~75 % comparing to the simple mode. The reason is that, with layered formation, the HTF bypasses the layers which are before and after the thermocline region causing no pressure drop incurred for these layers. The pressure drop gradually increases as the charge progresses. Experimental data presented in Fig. 13 also shows this trend but since the input pressure is not constant due to change in ambient conditions, the effect is not as much clear. The increase in pressure drop during charge is because of increasing region of the store behind the thermal front where the rate of heat transfer is slowed because of the nearly uniform temperature conditions *i.e.*, $T_g \approx T_s \approx T_c$ and reduced Re_m. This effect is dominant in simple mode. Reverse is observed during discharge as the store gradually reaches back to initial conditions prior to charge.

5.3. 1st Law efficiency

The 1st Law thermodynamic round-trip efficiency (RTE_{t1}) of the storage process can be defined here as the ratio of the heat recovered during discharge to the heat stored during charge, and is given by:

$$RTE_{t1} = \frac{Q_d}{Q_c} = \frac{\int_{t_c}^{t_d}\left[\dot{m}_g c_p \left(T_{top} - T_{bot}\right)\right] dt}{\int_0^{t_c}\left[\dot{m}_g c_p \left(T_{top} - T_{bot}\right)\right] dt} \tag{15}$$
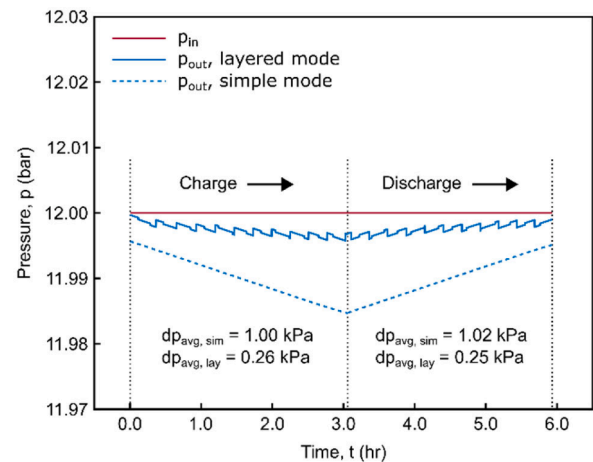

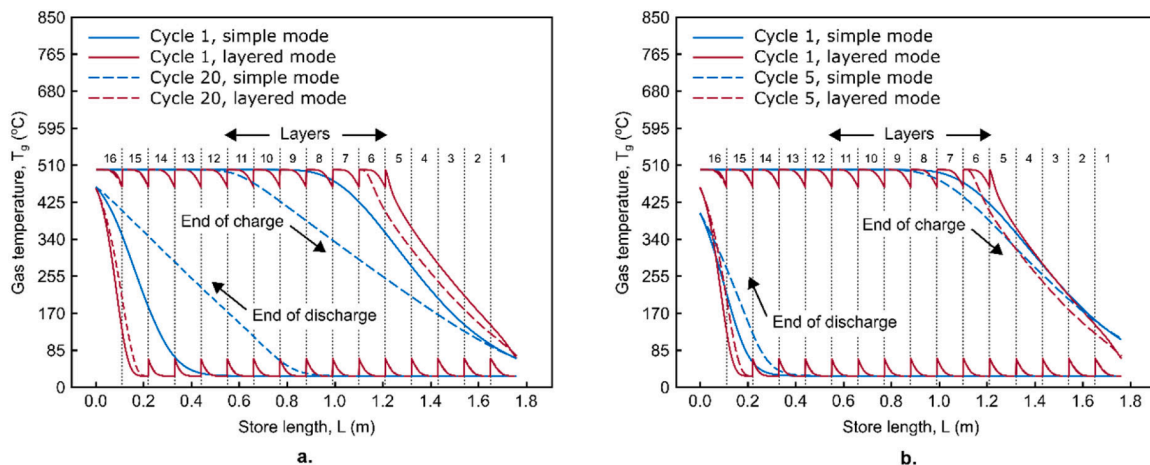**Fig. 15.** Comparison of pressure variation with time across HS for 1st cycle.

Fig. 14. Thermal fronts at the end of charge and discharge. Solid lines represent 1st cycle whereas dashed lines represent last cycle after reaching a steady state. **a.** scenario 1, and **b.** scenario 2.
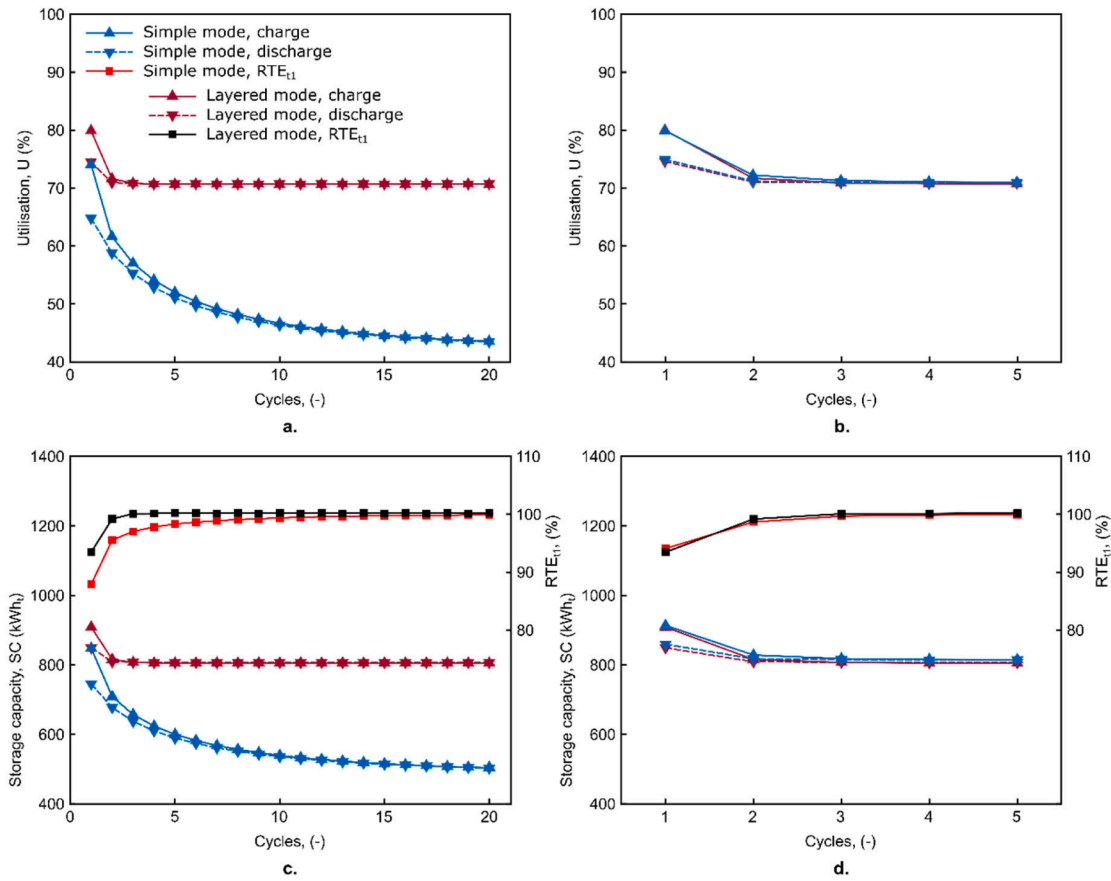
Fig. 16. Round-trip efficiency, storage capacity and utilization in a cyclic operation. **a.** & **c.** scenario 1, and **b.** & **d.** scenario 2.

Table 5
Summary of main results from 1st Law analysis.

	Mode	Simple		Layered
	Scenario	1	2	
1st cycle	RTE_{t1}, [%]	88.0	94.1	93.5
	SC_c, [kWh$_t$]	847.4	913.4	908.4
	SC_d, [kWh$_t$]	745.0	859.6	849.0
	U_c, [%]	75.2	81.0	80.6
	U_d, [%]	66.1	76.2	75.3
	t_c, [hr]	2.81	3.06	3.06
	t_d, [hr]	2.47	2.87	2.87
Steady-state cycle	RTE_{t1}, [%]	99.8	99.8	100.1
	SC_c, [kWh$_t$]	505.2	815.7	805.4
	SC_d, [kWh$_t$]	504.6	814.4	806.4
	U_c, [%]	44.8	72.4	71.4
	U_d, [%]	44.7	72.2	71.5
	t_c, [hr]	1.68	2.74	2.75
	t_d, [hr]	1.68	2.73	2.73

Fig. 16 shows RTE_{t1} along with storage capacity (SC) and utilisation (U) for both modes. Here, store utilisation is defined as the ratio of amount of energy stored or recovered per unit volume of store to its energy storage density, and is given by:

$$U_{c,d} = \frac{Q_{c,d}}{V \times \rho_{ES}} \tag{16}$$

For 1st cycle, the layered mode has the efficiency of 93.5 %, while the simple mode which yields 88.0 % and 94.1 % efficiencies in scenario 1 and 2 respectively. One factor that governs the efficiency is the value of t_c and t_d which directly depend on the adopted cycle control strategy. Since simple mode in scenario 2 and layered mode have the same t_c and t_d values, the results for the three performance indicators are nearly the same for the 1st and steady-state cycles, as given in Table 5. The main difference is found in the number of cycles to achieve the steady-state. Interestingly, RTE_{t1} approaches ~100 % in both modes for any scenario when steady-state has reached. The behaviour of the thermal front in simple mode for scenario 1, as discussed in *Sec.* 5.1, results in gradual deterioration of remaining two performance figures over the next cycles. The efficiency is increased but as the cyclic operation continues, the reducing t_c and t_d reduce both SC and U, as shown in Fig. 16.

5.4. 2nd Law efficiency

The 2nd Law round-trip exergy efficiency (RTE_{t2}) has also been evaluated in the present study and the calculation method is adopted from the previous study [73]. The fractional exergy or available work efficiency is defined as the ratio of net exergy stored during charge to net exergy recovered during discharge, and is given by:

$$RTE_{t2} = \frac{B_d}{B_c} = \frac{\int_{t_c}^{t_d} \left[\dot{m}_g c_p \left(T_{bot} - T_{top} - T_{amb} \ln\left(\frac{T_{bot}}{T_{top}}\right) \right) \right] dt}{\int_0^{t_c} \left[\dot{m}_g c_p \left(T_{top} - T_{bot} - T_{amb} \ln\left(\frac{T_{top}}{T_{bot}}\right) \right) \right] dt} \tag{17}$$

Various irreversible processes lead to exergy loss or destruction and hence the exergetic round-trip efficiency. In case of packed-bed thermal stores, the most important sources of irreversibility are due to inherent 'gas-solid' heat transfer taking place across a finite temperature difference, $\Delta T_{gs} = T_g - T_s$, HTF friction and rising T_g at store exit during charge which is unrecoverable upon discharge. We can define each source of irreversibility in terms of an exergy loss coefficient, ζ, defined as the fraction of exergy lost due to an entropy generating mechanism to the net exergy stored during charge, and is given by:

$$\zeta = \frac{T_{amb}}{B_c} \int_0^{t_c} \left(\dot{S}_{irr} \right) dt \tag{18}$$

where S_{irr} is the rate of instantaneous entropy generated due to irreversibility.

The exergetic loss coefficient due to gas–solid heat transfer across finite ΔT_{gs} is termed as thermal loss, ζ_t, and is given by:

$$\zeta_t = \frac{T_{amb}}{B_c} \int_0^{t_c} \left(\dot{S}_t \right) dt = \frac{T_{amb}}{B_c} \left[\int_0^{t_c} \left(\int \left(\frac{1}{T_s} - \frac{1}{T_g} \right) d\dot{Q} \right) dt \right] \tag{19}$$

The instantaneous rate of heat transfer, dQ, is given in Eq. (1).

The exergetic loss coefficient due to HTF friction is termed as pressure loss, ζ_p, and is given by:

$$\zeta_p = \frac{T_{amb}}{B_c} \int_0^{t_c} \left(\dot{S}_p \right) dt = \frac{T_{amb}}{B_c} \left[\int_0^{t_c} \left(\dot{m}_g R \ln \left(\frac{p_{top}}{p_{bot}} \right) \right) dt \right] \tag{20}$$

Finally, the exergetic loss coefficient due to increasing temperature of the HTF exiting the store towards the end of charge is termed as exit loss, ζ_x, and is given by:

$$\zeta_x = \frac{B_x}{B_c} = \frac{1}{B_c} \left[\int_0^{t_c} \left[\dot{m}_g c_p \left(T_{bot} - T_{hx} - T_0 \ln \left(\frac{T_{bot}}{T_{hx}} \right) \right) \right] dt \right] \tag{21}$$

where T_{hx} is the desired output temperature of HTF at the store exit during charge; this is also equal to discharge temperature, T_d, and is normally achieved using a heat exchanger.

These losses can be directly used to evaluate RTE_{t2} by using Eq. (22) below:

$$RTE_{t2} = 1 - (\zeta_t + \zeta_p + \zeta_x) \tag{22}$$

Table 6 presents the exergetic losses and corresponding round-trip efficiency. The values of the losses are accumulative *i.e.*, they have been calculated by integrating Eqs. (19–21) across the length of the store over complete duration of the charge. The cycle control strategy and simple mode scenarios were kept same as before. The results show that the value of RTE_{t2} falls in the range of 97–99 %. Steady-state cycle yield ~1% better efficiency compared with the 1st cycle for both modes. Of all the losses, ζ_t are the highest comparatively due to dominant gas–solid heat transfer-based irreversibility whereas ζ_p are the lowest.

These losses strictly depend on the transient performance of the store. Fig. 17 shows a comparison of instantaneous ζ_t and ζ_x in simple and layered mode operation. ζ_p have not been plotted as they are very small. Although the magnitude of ζ_p is remarkably small for any mode, the layered mode yields 80 % lesser losses compared with the simple mode, indicating the thermodynamic benefit of layering. ζ_t are significant and are very high in the early stages of charge and gradually

become smaller towards the end for the 1st cycle in any case. This is due to narrow and steep thermal front in the early stages where ΔT_{gs} is higher and the heat transfer takes place with smaller available heat transfer area. As the charge progresses, the thermal front becomes longer and thermal losses start to drop because of reduced ΔT_{gs}. For example, ζ_t drop from 97.93 % to 0.59 % and 1.11 % from start to the end of charge in simple and layered modes respectively (Fig. 17b). Upon discharge, this loss drops instantly from 4.6 % to 1.24 % and slowly increases to 3.17 % at the end in simple mode. In layered store, upon discharge, this loss drops from 2.2 % to 1.4 % and slowly increases to 4.72 %. The significantly smaller value of ζ_t at the onset of discharge compared to charge for both modes is again due to smaller ΔT_{gs}. Important to note here are that the spikes in the thermal loss curves for the layered mode are due to layer activation and deactivation causing abrupt variations in ΔT_{gs}. Fig. 17 also shows results plotted for steady-state cycles. It is noteworthy that the variation in spikes diminishes during charge when the layered mode reaches a steady-state operation.

As shown in Fig. 17, ζ_x remain zero for most part during charge and increase gradually when the nose of the thermal front starts to cross store exit. For an ideal store, $\zeta_x = 0$, but due to thermal irreversibilities it is never practically possible. If the store is a part of a PHES system, T_g at store exit is required to be brought back to T_{amb} through the use of a heat exchanger. On the contrary, the rising value of T_g at the store exit towards the end of charge can be used for any other heating purposes. As can be seen on Fig. 17a, in scenario 1 where the cycle control is 'temperature-based', both simple and layered modes produce nearly same instantaneous ζ_x at the end of charge i.e., 1.31 % and 1.35 % respectively in the 1st cycle. The sharp spikes in the curve for the layered mode can also be explained here similarly as before; as a particular layer reaches its end of charge stage, T_g increases at the store exit as the flow of gas is bypassed from next layers. Upon activation of the layer next in line, T_g at store exit drops suddenly to ambient because of active heat transfer taking place due to large ΔT_{gs} in the active layer. For simple mode in scenario 2, shown on Fig. 17b, the value of instantaneous ζ_x at the end of charge is 5.23 %, which is significantly higher compared with the corresponding value in scenario 1. The reason is that there is more time available for the simple mode in scenario 2 compared with scenario 1, allowing for gas to be issued from the store exit at a further increased temperature. Not much difference is observed in the behaviour of exit losses for steady-state cycles. Interestingly, there are no exit losses for any discharge period. However, an equivalent exit loss for discharge period may be calculated in a case where an external heat source is required at the store top to keep the exit gas temperature at T_c.

6. Conclusions

This paper studied hot packed-bed type thermal store both experimentally and numerically, focusing on its thermodynamic performance only. Previous studies have mostly considered hypothetical system design and operating conditions, and sensitivity analyses have been conducted accordingly. The main objective of the study was to experimentally observe the overall feasibility and difference in performance of the developed hot layered thermal store in comparison with its identical simple counterpart for use in a 600 kWh$_e$ Pumped Heat Energy Storage (PHES) demonstration system. Numerical model was validated by the experimental results. Further analysis was carried out to predict storage performance at design conditions.

The selection of using packed-bed type thermal storage in PHES system is not only due to the low cost, but also due to the benefit of direct heat transfer between working fluid and storage material, so that the heat transfer performance is the best and there is no need to use additional heat exchanger. The proposed system is scalable. The scale of such packed-bed should depend on the mass flow rate of the working fluid. Multiple systems can be used; however, the cost will be higher than a single larger system. Various publications and reports reveal that lack of experimental results from a real-scale system limit the prospect of
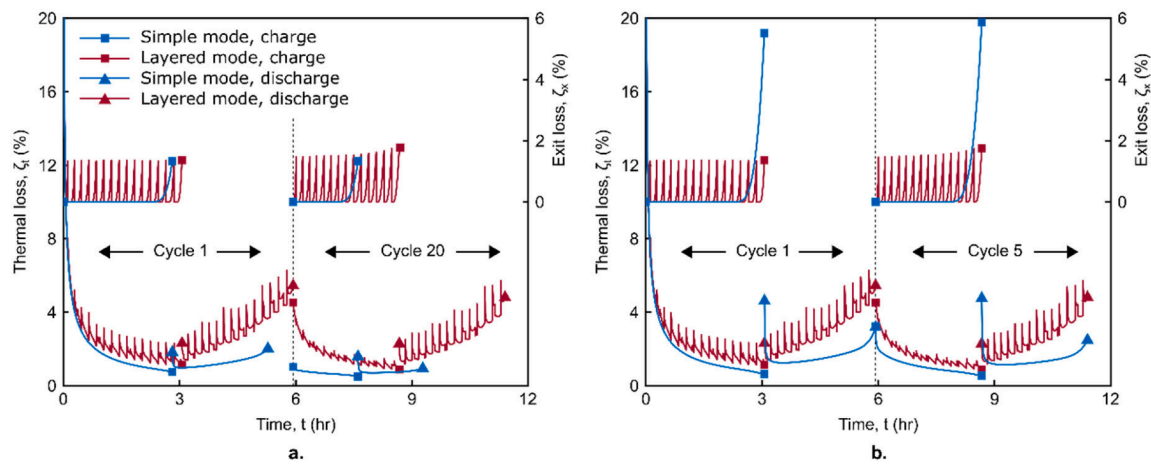
Table 6
Summary of results from 2nd Law analysis.

Mode	Scenario		Thermal loss ζ_t [%]	Pressure loss ζ_p [%]	Exit loss ζ_x [%]	Round-trip efficiency RTE_{t2} [%]
Simple	1	1st cycle	2.36	0.05	0.05	97.54
		Steady-state cycle	0.68	0.05	0.09	99.18
	2	1st cycle	2.22	0.05	0.29	97.44
		Steady-state cycle	1.07	0.05	0.37	98.51
Layered		1st cycle	2.77	0.01	0.21	97.01
		Steady-state cycle	1.67	0.01	0.35	97.97

Fig. 17. Comparison of variation of instantaneous thermal and exit losses over the charge and discharge durations for first and steady-state cycles. **a.** scenario 1, and **b.** scenario 2.

getting attention by the investors. It is therefore of utmost importance to practically realise a theoretically proposed solution and showcase the results to the scientific community. This initial demonstration of the layered packed-bed could eventually transform how packed-bed based energy storage was explored, for PHES, in particular. The experimental data will prove invaluable for further research. Main conclusions of the study are:

- Layered formation of storage media in a simple store results in reduced pressure drop; 64 % less pressure drop was confirmed experimentally at part-load conditions, and 75 % theoretically at full-load conditions.
- Layering improves thermal front shape but round-trip energy efficiency, storage capacity and utilization are not largely improved. The benefits are realized in terms of reduced pressure drop, faster reaching of steady-state cycle in a cyclic operation and maintaining a uniform temperature profile at the store exit for a longer period comparatively.
- With temperature-based cycle control, simple store yields comparable round-trip energy efficiency but because of reduced cycle durations, storage capacity and utilization efficiency are greatly compromised.
- With time-based cycle control, although simple and layered stores perform equally in terms of energy-based performance metrics, the exergy analysis showed that the exit losses in case of simple store will be slightly higher comparatively and, therefore, layered store will be a preferred choice.
- Exergy analysis further showed that in a cyclic operation, thermal losses decrease whereas exit losses increase over successive cycles for both simple and layered stores. However, pressure losses remain the same.

CRediT authorship contribution statement

Muhammad Tahir Ameen: Software, Formal analysis, Investigation, Writing - original draft. **Zhiwei Ma:** Conceptualization, Methodology, Writing - review & editing. **Andrew Smallbone:** Conceptualization, Investigation. **Rosemary Norman:** Conceptualization, Supervision. **Anthony Paul Roskilly:** Conceptualization, Supervision.

Declaration of Competing Interest

The authors declare that they have no known competing financial interests or personal relationships that could have appeared to influence the work reported in this paper.

Data availability

Data will be made available on request.

References

[1] IRENA. Renewable Energy Statistics 2022. Abu Dhabi: The International Renewable Energy Agency; 2022.
[2] Gielen D, Boshell F, Saygin D, Bazilian MD, Wagner N, Gorini R. The role of renewable energy in the global energy transformation. Energ Strat Rev 2019;24: 38–50.
[3] Barton JP, Infield DG. Energy storage and its use with intermittent renewable energy. IEEE Trans Energy Convers 2004;19:441–8.
[4] Luo X, Wang J, Dooner M, Clarke J. Overview of current development in electrical energy storage technologies and the application potential in power system operation. Appl Energy 2015;137:511–36.
[5] Castillo A, Gayme DF. Grid-scale energy storage applications in renewable energy integration: A survey. Energ Conver Manage 2014;87:885–94.
[6] Sawle Y, Gupta S, Bohre AK. Review of hybrid renewable energy systems with comparative analysis of off-grid hybrid system. Renew Sustain Energy Rev 2018; 81:2217–35.
[7] Chen H, Cong TN, Yang W, Tan C, Li Y, Ding Y. Progress in electrical energy storage system: A critical review. Prog Nat Sci 2009;19:291–312.
[8] Ajanovic A, Hiesl A, Haas R. On the role of storage for electricity in smart energy systems. Energy 2020;117473.
[9] World Energy Council. Energy Storage Monitor, Latest trends in energy storage; 2019.
[10] Irena. Electricity Storage and Renewables: Costs and Markets to 2030. Abu Dhabi: International Renewable Energy Agency; 2017.
[11] IEA (2021). Energy Storage, IEA, Paris https://www.iea.org/reports/energy-storage [accessed 25 June 2022].
[12] Steinmann W-D, Bauer D, Jockenhöfer H, Johnson M. Pumped thermal energy storage (PTES) as smart sector-coupling technology for heat and electricity. Energy 2019;183:185–90.
[13] Tiskatine R, Eddemani A, Gourdo L, Abnay B, Ihlal A, Aharoune A, et al. Experimental evaluation of thermo-mechanical performances of candidate rocks for use in high temperature thermal storage. Appl Energy 2016;171:243–55.
[14] Sarbu I, Sebarchievici C. A comprehensive review of thermal energy storage. Sustainability 2018;10:191.
[15] Gautam A, Saini R. A review on technical, applications and economic aspect of packed bed solar thermal energy storage system. J Storage Mater 2020;27:101046.
[16] Albert M, Ma Z, Bao H, Roskilly AP. Operation and performance of Brayton Pumped Thermal Energy Storage with additional latent storage. Appl Energy 2022; 312:118700.
[17] Chai L, Wang L, Liu J, Yang L, Chen H, Tan C. Performance study of a packed bed in a closed loop thermal energy storage system. Energy 2014;77:871–9.
[18] Al-Azawii MM, Theade C, Danczyk M, Johnson E, Anderson R. Experimental study on the cyclic behavior of thermal energy storage in an air-alumina packed bed. J Storage Mater 2018;18:239–49.

[19] Cheng X, Zhai X, Wang R. Thermal performance analysis of a packed bed cold storage unit using composite PCM capsules for high temperature solar cooling application. Appl Therm Eng 2016;100:247–55.

[20] Johnson E, Bates L, Dower A, Bueno PC, Anderson R. Thermal energy storage with supercritical carbon dioxide in a packed bed: Modeling charge-discharge cycles. J Supercrit Fluids 2018;137:57–65.

[21] Cárdenas B, Davenne T, Wang J, Ding Y, Jin Y, Chen H, et al. Techno-economic optimization of a packed-bed for utility-scale energy storage. Appl Therm Eng 2019;153:206–20.

[22] Zhao B-c, Cheng M-s, Liu C, Dai Z-m. Cyclic thermal characterization of a molten-salt packed-bed thermal energy storage for concentrating solar power. Appl Energy 2017;195:761–73.

[23] Tehrani SSM, Shoraka Y, Nithyanandam K, Taylor RA. Shell-and-tube or packed bed thermal energy storage systems integrated with a concentrated solar power: A techno-economic comparison of sensible and latent heat systems. Appl Energy 2019;238:887–910.

[24] Fasquelle T, Falcoz Q, Neveu P, Hoffmann J-F. A temperature threshold evaluation for thermocline energy storage in concentrated solar power plants. Appl Energy 2018;212:1153–64.

[25] Singh PL, Deshpandey S, Jena P. Thermal performance of packed bed heat storage system for solar air heaters. Energy Sustain Dev 2015;29:112–7.

[26] Bouadila S, Kooli S, Lazaar M, Skouri S, Farhat A. Performance of a new solar air heater with packed-bed latent storage energy for nocturnal use. Appl Energy 2013; 110:267–75.

[27] Singh H, Saini R, Saini J. A review on packed bed solar energy storage systems. Renew Sustain Energy Rev 2010;14:1059–69.

[28] Barbour E, Mignard D, Ding Y, Li Y. Adiabatic compressed air energy storage with packed bed thermal energy storage. Appl Energy 2015;155:804–15.

[29] He W, Wang J, Wang Y, Ding Y, Chen H, Wu Y, et al. Study of cycle-to-cycle dynamic characteristics of adiabatic Compressed Air Energy Storage using packed bed Thermal Energy Storage. Energy 2017;141:2120–34.

[30] Ortega-Fernández I, Zavattoni SA, Rodríguez-Aseguinolaza J, D'Aguanno B, Barbato MC. Analysis of an integrated packed bed thermal energy storage system for heat recovery in compressed air energy storage technology. Appl Energy 2017; 205:280–93.

[31] McTigue JD, White AJ, Markides CN. Parametric studies and optimisation of pumped thermal electricity storage. Appl Energy 2015;137:800–11.

[32] Desrues T, Ruer J, Marty P, Fourmigué J. A thermal energy storage process for large scale electric applications. Appl Therm Eng 2010;30:425–32.

[33] Wang L, Lin X, Chai L, Peng L, Yu D, Liu J, et al. Unbalanced mass flow rate of packed bed thermal energy storage and its influence on the Joule-Brayton based Pumped Thermal Electricity Storage. Energ Conver Manage 2019;185:593–602.

[34] Peng H, Shan X, Yang Y, Ling X. A study on performance of a liquid air energy storage system with packed bed units. Appl Energy 2018;211:126–35.

[35] Olympios AV, Sapin P, Freeman J, Olkis C, Markides CN. Operational optimisation of an air-source heat pump system with thermal energy storage for domestic applications. Energ Conver Manage 2022;273:116426.

[36] White AJ, McTigue JD, Markides CN. Analysis and optimisation of packed-bed thermal reservoirs for electricity storage applications. Proc Inst Mech Eng, Part A: J Power Energy 2016;230:739–54.

[37] Marti J, Geissbühler L, Becattini V, Haselbacher A, Steinfeld A. Constrained multi-objective optimization of thermocline packed-bed thermal-energy storage. Appl Energy 2018;216:694–708.

[38] Cascetta M, Cau G, Puddu P, Serra F. Numerical investigation of a packed bed thermal energy storage system with different heat transfer fluids. Energy Proc 2014;45:598–607.

[39] Al-Azawii MM, Theade C, Bueno P, Anderson R. Experimental study of layered thermal energy storage in an air-alumina packed bed using axial pipe injections. Appl Energy 2019;249:409–22.

[40] Anderson R, Shiri S, Bindra H, Morris JF. Experimental results and modeling of energy storage and recovery in a packed bed of alumina particles. Appl Energy 2014;119:521–9.

[41] Edwards J, Bindra H. An experimental study on storing thermal energy in packed beds with saturated steam as heat transfer fluid. Sol Energy 2017;157:456–61.

[42] McTigue J, White A. A comparison of radial-flow and axial-flow packed beds for thermal energy storage. Appl Energy 2018;227:533–41.

[43] Anderson R, Bates L, Johnson E, Morris JF. Packed bed thermal energy storage: A simplified experimentally validated model. J Storage Mater 2015;4:14–23.

[44] Bindra H, Bueno P, Morris JF, Shinnar R. Thermal analysis and exergy evaluation of packed bed thermal storage systems. Appl Therm Eng 2013;52:255–63.

[45] Esence T, Bruch A, Molina S, Stutz B, Fourmigué J-F. A review on experience feedback and numerical modeling of packed-bed thermal energy storage systems. Sol Energy 2017;153:628–54.

[46] Al-Azawii MM, Alhamdi SF, Braun S, Hoffmann J-F, Calvet N, Anderson R. Experimental study on packed-bed thermal energy storage using recycled ceramic as filler materials. J Storage Mater 2021;44:103375.

[47] Kocak B, Paksoy H. Performance of laboratory scale packed-bed thermal energy storage using new demolition waste based sensible heat materials for industrial solar applications. Sol Energy 2020;211:1335–46.

[48] Lai Z, Zhou H, Zhou M, Lv L, Meng H, Cen K. Experimental study on storage performance of packed bed solar thermal energy storage system using sintered ore particles. Sol Energy Mater Sol Cells 2022;238:111654.

[49] Zanganeh G, Pedretti A, Zavattoni S, Barbato M, Steinfeld A. Packed-bed thermal storage for concentrated solar power–Pilot-scale demonstration and industrial-scale design. Sol Energy 2012;86:3084–98.

[50] Singh S, Sørensen K, Condra T, Batz SS, Kristensen K. Investigation on transient performance of a large-scale packed-bed thermal energy storage. Appl Energy 2019;239:1114–29.

[51] Knobloch K, Muhammad Y, Costa MS, Moscoso FM, Bahl C, Alm O, et al. A partially underground rock bed thermal energy storage with a novel air flow configuration. Appl Energy 2022;315:118931.

[52] Trevisan S, Wang W, Guedez R, Laumert B. Experimental evaluation of an innovative radial-flow high-temperature packed bed thermal energy storage. Appl Energy 2022;311:118672.

[53] Rodrigues FA, de Lemos MJ. Discharge effectiveness of thermal energy storage systems. Appl Therm Eng 2022;209:118232.

[54] Le Roux D, Lalau Y, Rebouillat B, Neveu P, Olivès R. Thermocline thermal energy storage optimisation combining exergy and life cycle assessment. Energ Conver Manage 2021;248:114787.

[55] Wang L, Lin X, Zhang H, Peng L, Chen H. Brayton-cycle-based pumped heat electricity storage with innovative operation mode of thermal energy storage array. Appl Energy 2021;291:116821.

[56] Zhang H, Wang L, Lin X, Chen H. Technical and economic analysis of Brayton-cycle-based pumped thermal electricity storage systems with direct and indirect thermal energy storage. Energy 2022;239:121966.

[57] Zhang H, Wang L, Lin X, Chen H. Parametric optimisation and thermo-economic analysis of Joule-Brayton cycle-based pumped thermal electricity storage system under various charging–discharging periods. Energy 2023;263:125908.

[58] Zanganeh G, Commerford M, Haselbacher A, Pedretti A, Steinfeld A. Stabilization of the outflow temperature of a packed-bed thermal energy storage by combining rocks with phase change materials. Appl Therm Eng 2014;70:316–20.

[59] Galione P, Pérez-Segarra CD, Rodríguez I, Oliva A, Rigola J. Multi-layered solid-PCM thermocline thermal storage concept for CSP plants. Numerical Analy Perspect Appl Energy 2015;142:337–51.

[60] Cheng X, Zhai X. Thermal performance analysis and optimization of a cascaded packed bed cool thermal energy storage unit using multiple phase change materials. Appl Energy 2018;215:566–76.

[61] Liu Y-G, Zhang J-Y, Li H-J, Ji Q-Y, Zhou Q. Numerical study on stratification performance of cascaded three-layered packed-bed in the thermal storage process. Appl Therm Eng 2022;119669.

[62] Osterman K, Goswami DY. Effect of PCM fraction and melting temperature on temperature stabilization of hybrid sensible/latent thermal energy storage system for sCO2 Brayton power cycle. Energ Conver Manage 2021;237:114024.

[63] Xue X, Zhao C. Transient behavior and thermodynamic analysis of Brayton-like pumped-thermal electricity storage based on packed-bed latent heat/cold stores. Appl Energy 2023;329:120274.

[64] Crandall D, Thacher E. Segmented thermal storage. Sol Energy 2004;77:435–40.

[65] Howes JS, MacNaghten J, Hunt RG, Bennett RG, Wilson AB. Improved thermal energy storage apparatus. WO 2013/160650 A2; 2013.

[66] Bindra H, Bueno P, Morris JF. Sliding flow method for exergetically efficient packed bed thermal storage. Appl Therm Eng 2014;64:201–8.

[67] Mathur AK, Kasetty RB. Thermal energy storage system comprising optimal thermocline management. US 8,554,377 B2; 2013.

[68] Howes JS, MacNaghten J, Hunt RG. Improved heat storage apparatus. WO 2012/127178 A1; 2012.

[69] Geissbühler L, Mathur A, Mularczyk A, Haselbacher A. An assessment of thermocline-control methods for packed-bed thermal-energy storage in CSP plants, Part 1: Method descriptions. Sol Energy 2019;178:341–50.

[70] Geissbühler L, Mathur A, Mularczyk A, Haselbacher A. An assessment of thermocline-control methods for packed-bed thermal-energy storage in CSP plants, Part 2: Assessment strategy and results. Sol Energy 2019;178:351–64.

[71] Romero A, Chacartegui R, Garone E. Modeling, Simulation and Optimal Operation of Multi-Extraction Packed-Bed Thermal Storage Systems. Energies 2020;13:2247.

[72] McTigue JD, White AJ. Segmented packed beds for improved thermal energy storage performance. IET Renew Power Gener 2016;10:1498–505.

[73] McTigue JD, Markides CN, White AJ. Performance response of packed-bed thermal storage to cycle duration perturbations. J Storage Mater 2018;19:379–92.

[74] White A, McTigue J, Markides C. Wave propagation and thermodynamic losses in packed-bed thermal reservoirs for energy storage. Appl Energy 2014;130:648–57.

[75] Grosu Y, Faik A, Ortega-Fernández I, D'Aguanno B. Natural Magnetite for thermal energy storage: Excellent thermophysical properties, reversible latent heat transition and controlled thermal conductivity. Sol Energy Mater Sol Cells 2017; 161:170–6.

[76] Schumann TEW. Heat transfer: a liquid flowing through a porous prism. J Franklin Inst 1929;208:405–16.

[77] White AJ. Loss analysis of thermal reservoirs for electrical energy storage schemes. Appl Energy 2011;88:4150–9.

[78] Wakao N, Kaguei S, Funazkri T. Effect of fluid dispersion coefficients on particle-to-fluid heat transfer coefficients in packed beds: correlation of Nusselt numbers. Chem Eng Sci 1979;34:325–36.

[79] Holdich RG. Fundamentals of Particle Technology. Midland Information Technology and Publishing; 2002.

[80] Westrum Jr EF, Grønvold F. Magnetite (Fe3O4) heat capacity and thermodynamic properties from 5 to 350 K, low-temperature transition. J Chem Thermodyn 1969; 1:543–57.

[81] Grønvold F, Sveen A. Heat capacity and thermodynamic properties of synthetic magnetite (Fe3O4) from 300 to 1050 K. Ferrimagnetic transition and zero-point entropy. J Chem Thermodyn 1974;6:859–72.

[82] NIST-JANAF Thermochemical Tables, https://janaf.nist.gov/, [accessed 27 June 2022].